nature climate change

Article

https://doi.org/10.1038/s41558-024-01958-8

The emerging human influence on the seasonal cycle of sea surface temperature

Received: 31 May 2023

Accepted: 20 February 2024

Published online: 15 March 2024

Check for updates

Jia-Rui Shi [1] ✉, Benjamin D. Santer [1,2] ✉, Young-Oh Kwon [1] & Susan E. Wijffels[1]

Gaining insight into anthropogenic influence on seasonality is of scientific, economic and societal importance. Here we show that a human-caused signal in the seasonal cycle of sea surface temperature (SST) has emerged from the noise of natural variability. Geographical patterns of changes in SST seasonal cycle amplitude (SST_{AC}) reveal two distinctive features: an increase at Northern Hemisphere mid-latitudes related to mixed-layer depth changes and a robust dipole pattern between 40° S and 55° S that is mainly driven by surface wind changes. The model-predicted pattern of SST_{AC} change is identifiable with high statistical confidence in four observed SST products and in 51 individual model realizations of historical climate evolution. Simulations with individual forcings reveal that GHG increases are the primary driver of changes in SST_{AC}, with smaller but distinct contributions from anthropogenic aerosol and ozone forcing. The robust human 'fingerprint' identified here is likely to have wide-ranging impacts on marine ecosystems.

Earth's climate is simultaneously influenced by anthropogenic and natural external forcings, as well as by natural internal climate variability operating on a wide range of different spatial and temporal scales. Detection and attribution analysis seeks to disentangle these human and natural influences[1]. Pattern-based 'fingerprint' methods are a key component of detection and attribution studies. Such methods have successfully identified human fingerprints in long-term annual mean changes in surface and atmospheric temperatures[2–7], aspects of the hydrological cycle[8–12], atmospheric circulation[13,14] and ocean heat content[15,16].

The annual cycle is one of the most fundamental aspects of the climate and accounts for greater than 90% of seasonal temperature variability over most of the globe[17]. It influences human health, water supplies, agriculture, energy demand and ecosystems. Gaining insight into how anthropogenic forcing has impacted seasonality is of scientific, economic and societal importance. Although annual cycle changes have attracted recent scientific attention in detection and attribution studies[17–22], such investigations have not included ocean variables.

We focus here on changes in the amplitude of the annual cycle of sea surface temperature (SST_{AC}), which plays an important role in air–sea interactions, global rainfall patterns and the distributions of marine ecosystems[23–25]. In the tropical Pacific, model projections show an intensification of SST_{AC} in the twenty-first century compared with the twentieth century, which has been attributed to changes in meridional SST gradients[26] and atmospheric circulation[27]. In the mid-latitudes, SST_{AC} is projected to increase in both hemispheres[24,28,29]. These projections of SST_{AC} intensification in the mid-latitudes are consistent with the observed amplitude increase in the annual cycles of surface air temperature and tropospheric temperature[17,22] during recent decades. Given that SST, surface air temperature and tropospheric temperature are independently measured, the emergence of an externally forced signal in SST_{AC} would provide additional support for the identification of anthropogenic fingerprints in the annual cycles of surface air temperature and tropospheric temperature.

Several previous model investigations demonstrated that the mid-latitude amplification of SST_{AC} is primarily linked to changes in mixed-layer depth (MLD)[24,28–31]. In summer, decreasing MLD leads to trapping of the net surface heat flux in the ocean in a thinner layer, thereby yielding a larger summertime SST increase[28]. This shoaling of the mixed layer results from enhanced upper ocean stratification driven by ocean warming[32,33]. In simulations with estimated future GHG emissions, the annual mean mixed layer shoaling and the mid-latitude

[1]Woods Hole Oceanographic Institution, Woods Hole, MA, USA. [2]Joint Institute for Regional Earth System Science and Engineering, University of California Los Angeles, Los Angeles, CA, USA. ✉e-mail: jshi@whoi.edu; bensanter1289@gmail.com

SST_{AC} increase are projected to intensify[29] as the effective heat capacity of the thinner mixed layer decreases.

It is still unclear whether an anthropogenic fingerprint can be formally detected in the changing amplitude of the observed SST_{AC} and whether this fingerprint can be robustly attributed to human influence. We address this question here with four different observed SST datasets and over 50 individual model realizations of historical climate change. An important component of our fingerprint study is its use of idealized simulations and heat budget analysis to elucidate the physical mechanisms that dictate key features of the common model and observed patterns of SST_{AC} change.

Trends in SST_{AC}

In all four of the observed SST products we examined, SST_{AC} trends over our primary analysis period (1950–2014) increase in most ocean regions and have a similar spatial pattern (Fig. 1a–d). Some features of the observed pattern are also evident in model simulations of historical climate change (HIST; Fig. 1e). The changes common to the models and observations are dominated by zonal mean amplitude increases between 30° and 60° latitude in both hemispheres (Fig. 1f), poleward of the maxima in the SST_{AC} climatology (Extended Data Fig. 1). Another notable regional-scale feature of the SST_{AC} trends in the HIST multi-model mean (MMM) and the observed Hadley Center Sea Ice and SST dataset version 1 (HadISST) and Program for Climate Model Diagnosis and Intercomparison SST dataset (PCMDI) is the decrease in annual cycle amplitude in the vicinity of the Antarctic Circumpolar Current (Fig. 1e) south of 50° S.

Although models can reproduce the positive observed SST_{AC} trends at Northern Hemisphere mid-latitudes, the observed trends are smaller than in the simulations (Fig. 1f). One possible interpretation of this result is that the observed regional signals may be partly suppressed by the specific phasing of internal variability in the North Atlantic, as is the case with observed annual mean warming in the tropical Pacific[34,35]. Differences between SST_{AC} trends in the observed data and the HIST MMM are also prominent in the tropics, such as the pronounced maximum in the western equatorial Pacific that appears only in observations.

These model–observation differences may be partly due to the fact that the MMM is an average over individual realizations of historical climate change (in a single model) and an average over models. Averaging damps the noise of natural internally generated variability, which is uncorrelated across model realizations (except by chance). The MMM should therefore more clearly reveal the response to external forcing[34,35]. In contrast, there is only one realization of the observed record, which contains both internal variability and the forced signal in SST_{AC}. We therefore expect observed SST_{AC} changes to be noisier than in the MMM, particularly in regions where multidecadal variability affects tropical and subtropical temperature trends[34,35].

Could the above-mentioned model–observation differences in SST_{AC} trends be related to model biases in climatological mean SST_{AC} patterns? We found that the model-average correlation between the patterns of model biases in the climatology of SST_{AC} and the model biases in the patterns of trends of SST_{AC} was low ($R = 0.06$). We inferred from this that model biases in climatology are unlikely to be a dominant factor in explaining the differences between the observed and simulated SST_{AC} trend patterns in Fig. 1a–d and Fig. 1e. This does not, however, rule out a possibility we discuss later—that overestimated climate sensitivity may contribute to model–observation differences in SST_{AC} trends[36].

The MMM and observations show closer agreement in global-scale features of the zonally averaged SST_{AC} trends (Fig. 1f), with a common pattern of larger increases in the amplitude of SST_{AC} in the extratropics relative to the tropics. This pattern occurs in both hemispheres, but the mid-latitude increases in SST_{AC} are larger and broader in the Northern Hemisphere than in Southern Hemisphere. This hemispheric asymmetry is consistent with results from previous studies of changes in the amplitude of the annual cycle of mid-tropospheric temperature[17,22]. As noted above, the simulated decrease in SST_{AC} trends in the Southern Ocean (Fig. 1f) is common to HadISST and PCMDI. Although the other two observational estimates do not show negative SST_{AC} trends between 50° S and 60° S, they have trend magnitudes within this latitude band that are smaller than the positive trends between 35° S and 45° S, and thus are consistent with the MMM results in a relative sense.

Fingerprint analysis and detection time

We used a standard pattern-based method to determine whether the model-predicted externally forced fingerprint of SST_{AC} changes is statistically identifiable in observations[37]. The fingerprint we searched for is the leading empirical orthogonal function (EOF) of the MMM SST_{AC} anomalies (Methods). The fingerprint is calculated from the HIST simulations over the period 1950–2014 (Fig. 2a). Our analysis assumed that the spatial structure of the fingerprint pattern did not change markedly over time[17,38]. We tested and confirmed this assumption by calculating the HIST fingerprint for four different analysis periods (1950–2014, 1960–2014, 1970–2014 and 1980–2014; Extended Data Fig. 2).

We compared the time-invariant SST_{AC} fingerprint pattern calculated from the HIST MMM with the time-evolving SST_{AC} patterns from observed datasets and long model control runs, respectively. These comparisons yielded time series of similarity between the fingerprint and observed SST_{AC} patterns and between the fingerprint and patterns of natural internal variability in SST_{AC}. By varying the trend length L over a range of timescales (from 10 to 65 years), we could determine whether (and when) the similarity between the observations and the HIST fingerprint showed a statistically significant signal—that is, an increase in pattern similarity over time that is unlikely to be due to natural internal variability alone.

Timescale-dependent signal-to-noise (S/N) ratios were calculated from the trends of these signal and noise time series (Fig. 2b). We stipulated that fingerprint detection occurred at trend length L if the S/N ratio exceeded a 5% significance threshold and remained above this threshold for all trend lengths larger than L. The model HIST fingerprint was identifiable with high statistical confidence (that is, at the 5% significance level or better) in all four observational SST datasets after approximately 2000. At the end of the 65 yr record, S/N ratios in the observations varied between 2.8 and 3.5. This indicates that smaller-scale differences between the four observational datasets (such as the previously noted SST_{AC} trend differences at high latitudes in the Southern Hemisphere) have relatively small impact on detection of the global-scale fingerprint in observations.

We also show the S/N ratios obtained when the HIST MMM fingerprint was searched for in individual realizations of HIST simulations (grey curves in Fig. 2b). In all 51 realizations, S/N ratios exceeded the 5% threshold before the end of the simulation period in 2014. As in the case of the observations, SST_{AC} changes in individual HIST runs exhibited time-increasing similarity with the fingerprint, pointing towards the robustness of the model-predicted forced SST_{AC} response.

The S/N ratios calculated with observed data were generally within, but close to the lower end of, the model-generated S/N ratio distribution. There are multiple (not mutually exclusive) possible explanations for this result. These include errors in the model external forcings[39], errors in the simulated SST_{AC} responses to the applied forcings, residual systematic errors in the observations and model–observation mismatches in the random phasing of internal variability (for example, the El Niño/Southern Oscillation, Interdecadal Pacific Oscillation and Pacific Decadal Oscillation). The latter explanation contributes to the more muted observed annual mean tropospheric warming over the satellite era[34].

It is still unclear, however, what influence such mismatches in simulated and observed variability phasing have on changes in the

https://doi.org/10.1038/s41558-024-01958-8

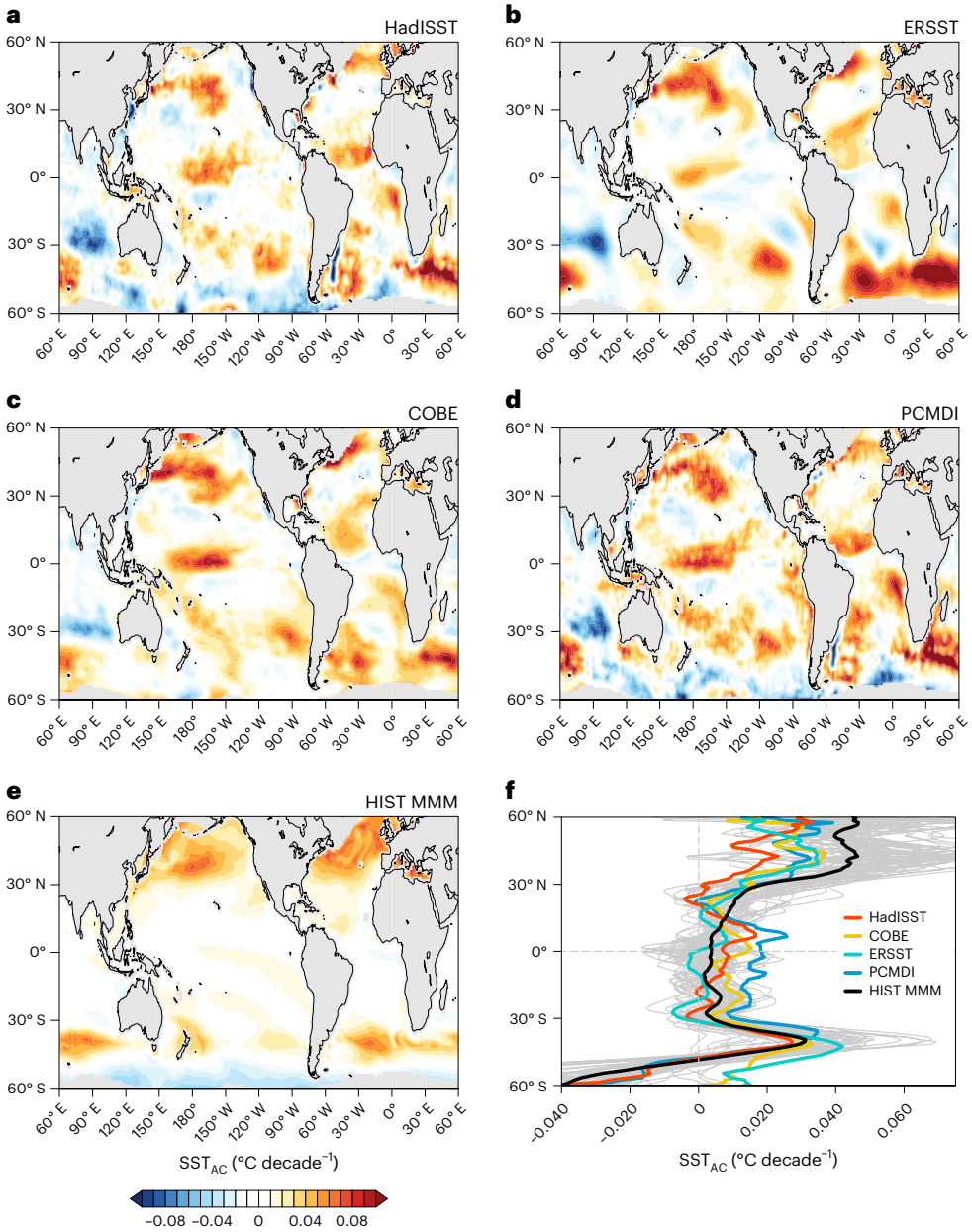

Fig. 1 | Trends in SST$_{AC}$ over the period 1950–2014. a–d, Trends from the observed HadISST (**a**), the NOAA Extended Reconstructed SST dataset version 5 (ERSST) (**b**), the Centennial in situ Observation-Based Estimates of the variability of SST and marine meteorological variables, version 2 (COBE) (**c**) and PCMDI (**d**) datasets. **e**, Trends from the MMM of HIST simulations from the Coupled Model Intercomparison Project Phase 6 (CMIP6). Regions where the model-average climatological sea-ice coverage is greater than 10% are masked in grey. **f**, Zonal mean trends in the amplitude of the SST$_{AC}$ estimated from observations and models. The grey curves are from 51 individual HIST simulations. The domain over which all calculations are performed is restricted to 60° S–60° N to minimize the impact of sea-ice changes on SST$_{AC}$. The colour scale in **e** also applies to **a–d**.

seasonal cycle of SST. Here we note that individual ensemble members generated with the same model and external forcings can have appreciable differences in their S/N behaviour (Extended Data Fig. 3). This suggests that, as in the case annual mean tropospheric temperature changes[34], model–observation differences in the phasing of internal variability may have marked influence on SST$_{AC}$, and hence on the overestimated 'model-only' S/N ratios in Fig. 2b. The non-negligible correlation between climate sensitivity[40] and the model-only S/N ratios over the full 65 yr analysis period (R = 0.55) provides evidence that overestimated model climate sensitivity[36] could also contribute to overestimated model-only S/N ratios (Extended Data Fig. 4).

It is important to determine the monitoring period required to identify the model-predicted HIST SST$_{AC}$ fingerprint. As in the case of Fig. 2b, this is the trend length L at which detection occurs, shown as a function of the choice of the analysed period (Fig. 2c). We considered four different periods; each ended in 2014 but had a different start date (1950, 1960, 1970 and 1980). There were two principal findings from this analysis. First, irrespective of the assumed start date of monitoring, the model-predicted HIST SST$_{AC}$ fingerprint pattern in Fig. 2a was robustly identifiable in all four observed SST datasets and in all 51 model realizations of historical climate change. Except in the case of S/N ratios obtained with COBE data, the observed values of L were always contained within the spread of the model results.

Second, a common feature of both the simulated and observed results is that L decreases systematically with later start dates. For the MMM SST$_{AC}$ changes, L was approximately 48 years and 18 years for

https://doi.org/10.1038/s41558-024-01958-8

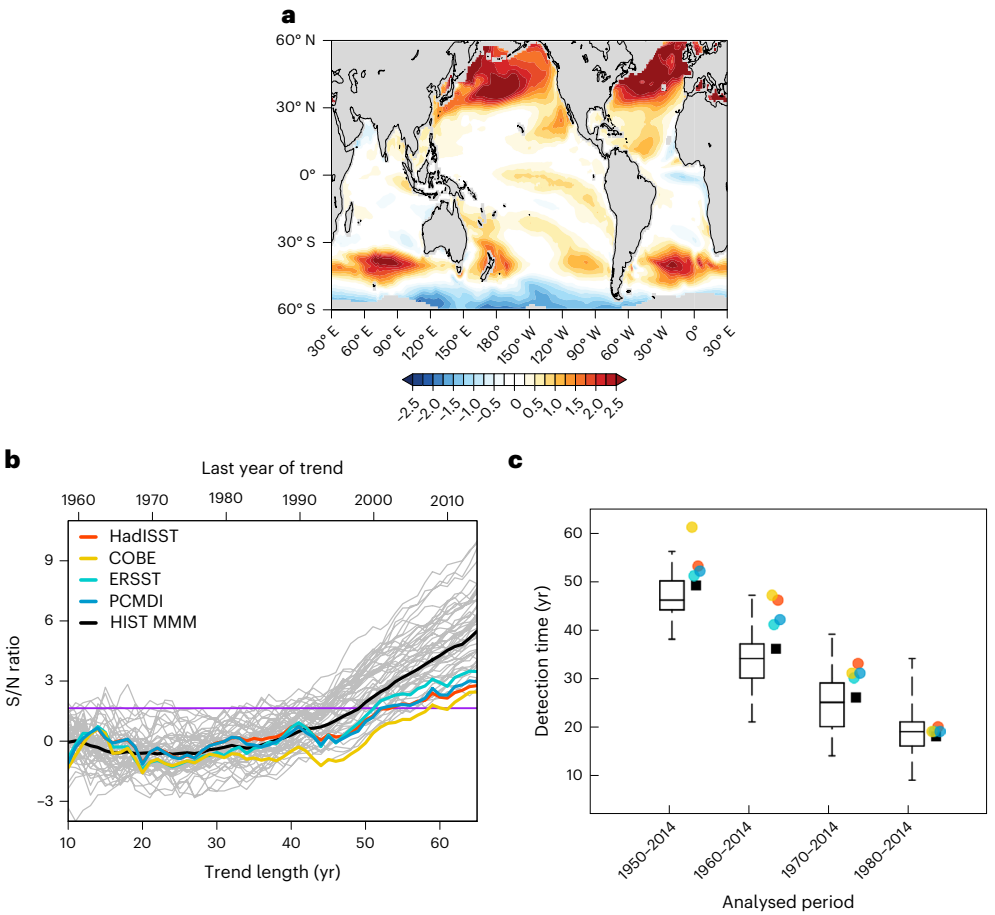

Fig. 2 | SST_{AC} fingerprint and S/N ratio analyses. a, Time-invariant HIST MMM fingerprint pattern. The fingerprint is defined here as the EOF1 of the MMM SST_{AC} changes over the period 1950–2014 (the explained variance is 36.9%). **b**, Timescale-dependent S/N ratios for trends calculated from signal and noise time series for 1950–2014. The HIST MMM result is the black curve; results from individual HIST runs are the grey curves. The coloured lines denote S/N ratios estimated by searching for the HIST MMM SST_{AC} fingerprint in four different observed SST datasets. The horizontal purple line is the 5% significance level (Methods). **c**, Detection time relative to the start year for the model-predicted SST_{AC} fingerprint from the HIST experiment. Fingerprint detection occurs when the S/N ratios for an L-year analysis period first exceed the stipulated significance level and then remain above it for all larger values of L. The y axis shows the value of L that satisfies this condition. Results are for four different assumed analysis start years (1950, 1960, 1970 and 1980). In the box and whisker plots, the horizontal bar is the median value, the box size represents the interquartile range and the whiskers span the full range of detection times from all 51 individual HIST realizations. Black squares are the detection times calculated with the MMM. Coloured circles are detection times estimated by searching for the model-predicted SST_{AC} fingerprint in four different observed SST datasets (see the legend in **b**).

start dates in 1950 and 1980 (respectively). This systematic decrease is probably due to larger net positive anthropogenic forcing over the 1980–2014 period than over periods with earlier start dates that sample appreciable negative forcing by anthropogenic aerosols. As will be shown in the next section, GHG forcing is the dominant influence on simulated SST_{AC} changes, so changes over time in the relative importance of GHG and anthropogenic aerosol forcing must contribute to the differences in L in the four analysis periods in Fig. 2c. Note that for fingerprint detection in the four different observed SST datasets, the spread in L values decreased as a function of increasing start date. This decrease in spread is partly due to improvements over time in the quality and spatial coverage of SST measurements and overlap between datasets.

Contributions from individual external forcings

We used single-forcing simulations to isolate and quantify the individual contributions of changes in well-mixed GHGs, anthropogenic aerosols (AER), stratospheric ozone depletion (O3) and volcanic eruptions and solar variability (NAT) (Methods). We applied two different methods to understand the effects of single forcings: (1) to estimate the contributions of individual external forcings to the time-evolving S/N ratios obtained with the HIST MMM fingerprint, the GHG, AER, O3 and NAT single-forcing simulations were all regressed onto the same HIST fingerprint used in the previous section; (2) to determine whether the model-predicted fingerprint associated with an individual forcing was statistically identifiable, SST_{AC} changes from observations and HIST runs were projected onto each of the four fingerprints estimated from the GHG, AER, O3 and NAT single-forcing experiments. Here we focus on Method 1 results. The results based on Method 2 are discussed in the Methods.

The S/N results for Method 1 indicate that GHG forcing is the dominant contributory factor to the identification of the HIST SST_{AC} fingerprint, which is detectable in the GHG MMM before 1990 (and before the end of the analysis period in 2014 in 48 out of 51 individual GHG realizations; Extended Data Fig. 5). The S/N ratios for the 'GHG only' case increase nearly linearly with increases in L and the magnitude of the GHG forcing. In contrast, S/N results for AER show markedly nonlinear behaviour as L increases. This is due to non-monotonic changes in emissions of anthropogenic sulfate aerosols, with large emissions after World War II followed by a reduction in emissions from North America and Europe after the 1980s[41–43]. The HIST SST_{AC} fingerprint was not detectable in the MMM of AER, O3 or NAT.

https://doi.org/10.1038/s41558-024-01958-8

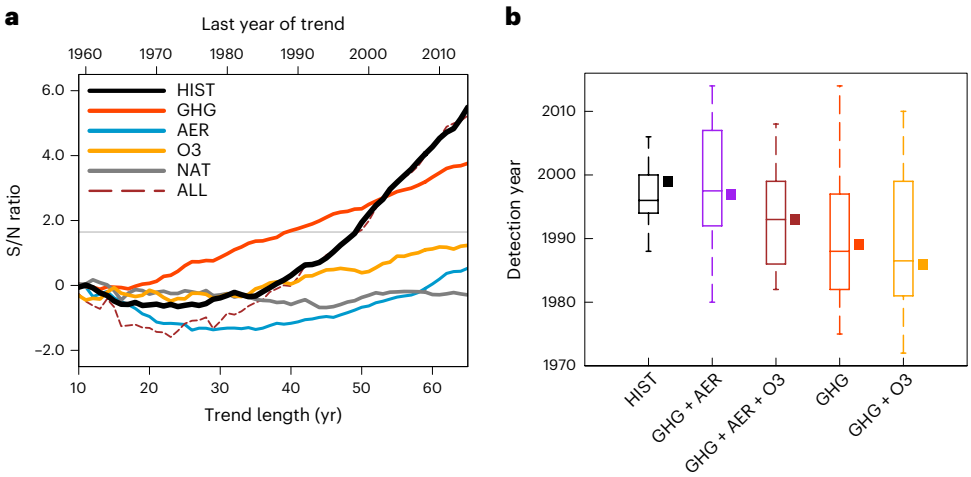

Fig. 3 | S/N ratios and detection times from single-forcing runs and their linear combinations. a, S/N ratios for the signal trends obtained by fingerprint analyses involving the patterns of SST_{AC} change estimated from the MMM of different experiments. Results are for Method 1 (Methods). For O3, the MMM is calculated from the four models for which O3 results were available. The MMM in the remaining cases is based on a larger set of ten models. ALL represents the linear combination of S/N ratios from GHG, AER, O3 and NAT. The horizontal grey line is the 5% significance level. **b**, The detection year of the HIST fingerprint estimated from HIST, GHG and linear combinations of SST_{AC} changes from GHG, AER and O3. The analysis period is 1950–2014. In the box and whisker plots, the horizontal bar is the median value, the box size represents the interquartile range and the whiskers span the full range of detection times from all the analysed model simulations.

Our analysis of the impact of individual anthropogenic factors assumed additivity of the forced responses in GHG, AER, O3 and NAT[44,45]. To test the validity of this additivity assumption, we compared the HIST S/N results in Fig. 3a with S/N results obtained for ALL, the linear combination of the individual S/N ratios obtained for the GHG, AER, O3 and NAT experiments. Additivity is a reasonable assumption for analysis periods longer than 40 years. For periods shorter than 40 years, differences between the HIST and ALL S/N results are probably related to the combined effects of larger noise on shorter timescales, the smaller ensemble size for O3 and nonlinear aspects of the forced SST_{AC} responses[46–48].

The detection year for the SST_{AC} fingerprint differed across HIST, GHG and three linear combinations of individual SST_{AC} responses (GHG + AER, GHG + O3 and GHG + AER + O3; Fig. 3b). The primary influence on detection year was GHG, with AER acting to delay fingerprint detection: 'GHG only' yielded systematically earlier detection year than any set of SST_{AC} changes that includes AER (HIST, GHG + AER and GHG + AER + O3). Including O3 also advanced detection time, with the earliest median detection year of the HIST SST_{AC} fingerprint (in 1985) in the GHG + O3 linear combination. The spread in detection year obtained with linear combinations was larger than the spread in detection year inferred from HIST. This is probably due to amplification of noise in the linear combination of individual responses.

Physical drivers of SST changes

Here we seek to understand the physical drivers of the SST_{AC} changes described in the previous sections. In the observations, warming of zonal mean SST over 1950–2014 occurred in nearly all months and latitudes (Extended Data Fig. 6). This was more pronounced in the mid-latitudes of the summer hemisphere. In the Southern Hemisphere at approximately 40° S, both the observations and HIST displayed warming relative to annual mean trends in austral summer and cooling relative to annual mean trends in austral winter (Fig. 4a,b). In HIST, this feature was primarily driven by GHG forcing (Fig. 4c). Relative to observations, CMIP6 models yielded larger Northern Hemisphere temperature rises in both summer and winter. As noted above, there are multiple possible interpretations of this result.

Another prominent aspect of HIST and GHG was a dipole pattern characterized by anticorrelation between the seasonal temperature changes at roughly 40° S and 55° S. GHG and O3 forcing both contributed to this feature (Fig. 4c,d). As noted above, this dipole was evident in two of the four observed datasets (HadISST and PCMDI; Extended Data Fig. 7). These observational differences probably arise because satellite data were included in HadISST and PCMDI, but not in ERSST and COBE. In consequence, the Southern Ocean is better represented in the first two datasets, especially in the vicinity of sea ice.

Buoyancy flux and wind stress changes are two major surface forcings affecting the Southern Ocean climate[49–51]. We explored the respective effects of buoyancy (dominated by heat flux change) and wind (momentum) forcing on SST_{AC} changes using the Flux-Anomaly-Forced Model Intercomparison (FAFMIP) experiments (Fig. 5). In the FAF-stress experiment, in which CO_2-induced perturbations to the ocean are imposed in wind stress only, the Southern Hemisphere mid-latitudes showed a robust meridional dipole pattern in zonal mean SST_{AC} change (Fig. 5b). In the FAF-heat experiment, CO_2-driven perturbations to heat fluxes amplified SST_{AC} in both hemispheres, but the magnitude of the change is markedly larger in the Northern Hemisphere (Fig. 5c), where the wind stress effect is limited. The FAFMIP results imply that wind forcing caused by CO_2 increases is the main driver of the above-described SST_{AC} dipole pattern between 40° S and 55° S found in HIST, GHG and two of the observed SST datasets. In contrast, changes in Northern Hemisphere mid-latitude SST_{AC} arise from increased surface heat flux linked to atmospheric warming.

In addition to the influence of surface wind stress and heat flux forcings, the SST_{AC} fingerprint can also be influenced by ocean adjustments arising from MLD changes. We investigated the role of MLD changes with a simplified mixed-layer heat budget analysis of the HIST runs. Our heat budget model also considered the effects of the net surface heat flux (Qnet) and shortwave radiation flux out of the mixed-layer base into the intermediate ocean (Qb) (Methods; equation (3)). The patterns of the annual cycle amplitude of SST tendency ($dSST/dt_{AC}$) change in the HIST runs can be reproduced by this simple model (Fig. 6a,b) and are consistent with the SST_{AC} fingerprint (Fig. 2a). The shoaling of MLD with fixed Qnet − Qb is the key factor here (Fig. 6c). In winter, this shoaling effect generates SST cooling by enhancing the temperature response to winter heat loss. In summer, shoaling yields SST warming. Our heat budget analysis helps to explain the previously described findings based on the analysis of the HIST and FAFMIP

https://doi.org/10.1038/s41558-024-01958-8

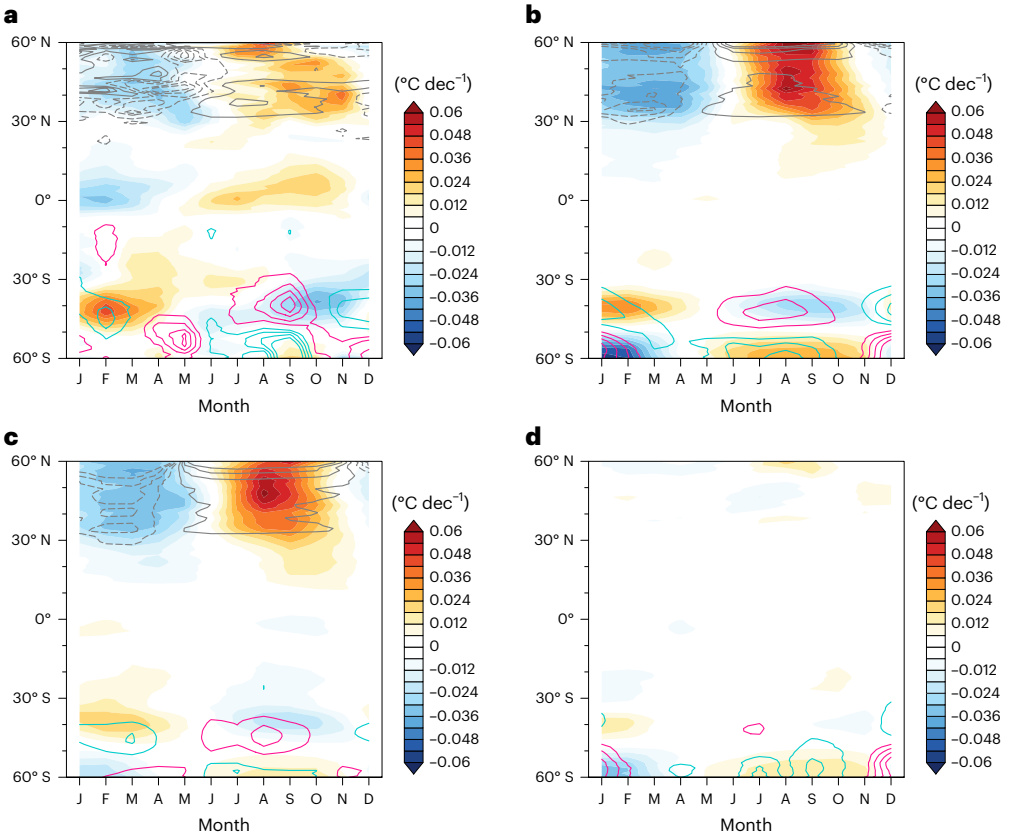

Fig. 4 | Zonal mean trends over 1950–2014 in monthly mean SST, zonal wind stress and MLD. a, The ensemble mean of four different observed datasets. **b**–**d**, The MMM of the HIST, GHG and O3 simulations. All results are departures from annual mean trends. Coloured shading denotes monthly SST trends, grey contours are MLD trends plotted with 0.75 m dec^{-1} intervals and coloured contours are zonal wind stress trends plotted with 7.2 × 10^{-4} Pa dec^{-1} intervals (with positive changes shown in magenta). The zero contours are omitted. We show the MLD changes in the Northern Hemisphere only, and the wind stress changes in the Southern Hemisphere only. Additional information about simulated and observed MLD and wind changes (including observational data sources) is given in Extended Data Fig. 9.

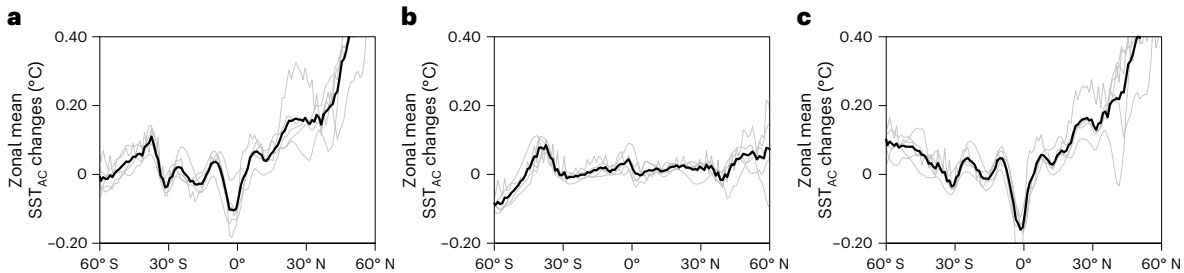

Fig. 5 | Zonal mean SST$_{AC}$ changes from FAFMIP perturbation experiments relative to pre-industrial control simulations. a–**c**, Results from FAF-all (**a**), FAF-stress (**b**) and FAF-heat (**c**). For each model, the pre-industrial control (piControl) results are averaged over the full length of the simulation. Perturbation results are averaged over years 31 to 70. The grey curves are from individual models and the black curves are the MMM results.

runs, showing that MLD changes are an important component of the response to the surface heat flux changes.

As a result of this seasonally dependent effect of the MLD shoaling, SST$_{AC}$ would be amplified even with constant MLD shoaling throughout the year. This is why both hemispheres show positive annual cycle changes in the 30–50° latitude band. Between 50° S and 60° S, the MLD deepens in austral summer, which appears to overwhelm the shoaling of MLD in austral winter, thus decreasing SST$_{AC}$ in this band. The fixed MLD case resulted in a weak, but reduced, SST$_{AC}$ in most regions (Fig. 6d), which implies that the warming induced by the Qnet-Qb change is slightly larger in winter than in summer.

We performed two further sensitivity experiments: (1) constant monthly MLD shoaling, in which the summer value was applied for all 12 months at each location; and (2) shoaling MLD by 5% in every month and location relative to the background monthly value. Our results suggest that the absolute change and relative change of MLD give rise to similar patterns (Extended Data Fig. 8). The major difference was in the 50–60° S band, apparently due to the opposite directions of MLD change between austral winter and summer (Extended Data Fig. 9a,b). For all other latitudes, the shoaling of the mixed layer was consistent with seasons.

The westerly wind stress in the 50–60° S region increases in austral summer (Extended Data Fig. 9c,d). This can deepen MLD by increased

https://doi.org/10.1038/s41558-024-01958-8

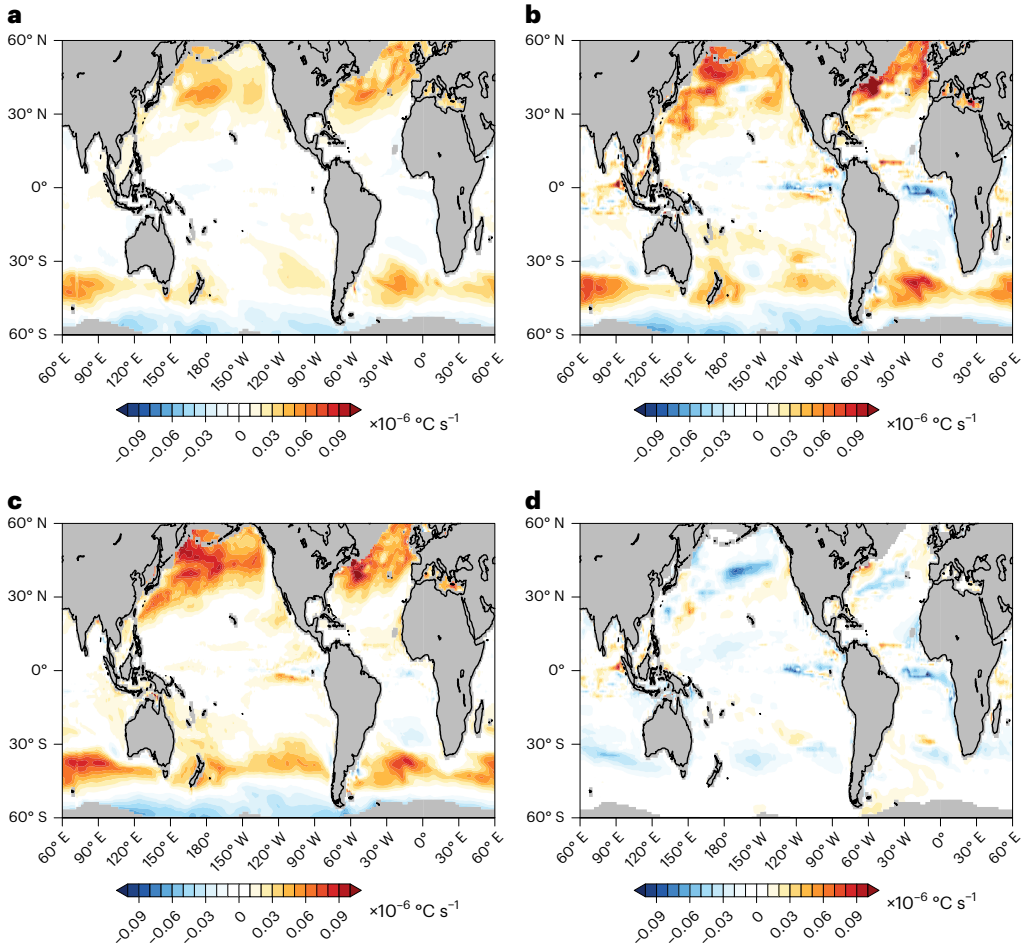

Fig. 6 | Changes in annual cycle of SST tendency between 1950–1979 and 1985–2014. a,**b**, Changes in annual cycle of SST tendency from CMIP6 HIST MMM (**a**) and the estimate based on the mixed-layer heat budget model (**b**). **c**,**d**, Contributions of the changing MLD (**c**) and heat flux (Qnet − Qb) (**d**) to the changes in the annual cycle of SST tendency, respectively.

local turbulent mixing, as well as by the increased equatorward advection of colder water. The negative wind stress changes between 30° S and 50° S have the opposite effect. The contrasting surface wind responses in the 30–50° S and 50–60° S bands reflect the poleward shifting of zonal winds over the Southern Ocean caused by GHG and O3 forcing (Fig. 4c,d). This shift is consistent with the FAF-stress response to CO_2-driven wind stress changes.

Conclusions

Most previous studies of SST_{AC} focused primarily on projected twenty-first-century changes[29,31]. Here we examined whether there is a detectable fingerprint pattern of human-induced SST_{AC} change over the period 1950–2014. We provide scientific evidence that a human-caused SST_{AC} signal has already emerged from the background noise of natural variability. Geographical patterns of SST_{AC} changes show increased SST_{AC} at mid-latitudes in the Northern Hemisphere and a distinctive meridional dipole structure at Southern Hemisphere mid-latitudes. These large-scale zonal features are common to observations and model simulations with anthropogenic forcing, and are dissimilar to the smaller-scale structure of natural internal variability. This helps to explain why the model-estimated SST_{AC} fingerprint in response to combined anthropogenic and natural external forcing is identifiable by the end of the twentieth century in all four observed SST datasets analysed here. The fingerprint is also robustly identifiable in all 51 model realizations of historical climate change.

Single-forcing experiments indicated that increases in well-mixed GHGs are the dominant factor in the identification of externally forced changes in SST_{AC}. Anthropogenic aerosol emissions are likely to have delayed the detection of this fingerprint by approximately 7–8 years on average. External forcing from stratospheric ozone depletion partially contributed to the development of the SST_{AC} dipole structure at Southern Hemisphere mid-latitudes, whereas natural external forcing by volcanoes and solar irradiance changes had relatively little effect on the detection of a human fingerprint in SST_{AC}.

Model simulations and a heat budget analysis revealed that the leading physical drivers of these large-scale SST_{AC} changes are different in the two hemispheres. In the Southern Hemisphere, the impacts of changes in atmospheric circulation and surface wind stress on the MLD are the key determinant of the dipole-like SST_{AC} response in the Southern Ocean. In the mid-latitudes of both hemispheres, human-induced warming yields increased stratification of the upper ocean, which in turn causes a reduction of the MLD during all seasons. Year-round mixed-layer shoaling decreases its thermal inertia, thereby amplifying the mid-latitude SST_{AC}.

Human-driven amplification of the mid-latitude seasonal cycle of SST has important implications for future changes in the behaviour of marine ecosystems. The SST changes found here have the potential to influence both the productivity and distribution of marine species that constitute key food resources for human societies. Our finding of robust changes in the seasonality of SST should motivate more detailed exploration of the anthropogenically forced seasonal changes in a wide range of different ocean properties.

Online content

Any methods, additional references, Nature Portfolio reporting summaries, source data, extended data, supplementary information, acknowledgements, peer review information; details of author contributions and competing interests; and statements of data and code availability are available at https://doi.org/10.1038/s41558-024-01958-8.

References

1. Bindoff, N. L. et al. in *Climate Change 2013: The Physical Science Basis* (eds Stocker, T. F. et al.) 867–952 (IPCC, Cambridge Univ. Press, 2014).
2. Hegerl, G. C. et al. Detecting greenhouse-gas-induced climate change with an optimal fingerprint method. *J. Clim.* **9**, 2281–2306 (1996).
3. Santer, B. D. et al. A search for human influences on the thermal structure of the atmosphere. *Nature* **382**, 39–46 (1996).
4. Tett, S. F. B., Mitchell, J. F. B., Parker, D. E. & Allen, M. R. Human influence on the atmospheric vertical temperature structure: detection and observations. *Science* **274**, 1170–1173 (1996).
5. Stott, P. A. et al. External control of 20th century temperature by natural and anthropogenic forcings. *Science* **290**, 2133–2137 (2000).
6. Santer, B. D. et al. Quantifying stochastic uncertainty in detection time of human-caused climate signals. *Proc. Natl Acad. Sci. USA* **116**, 19821–19827 (2019).
7. Santer, B. D. et al. Exceptional stratospheric contribution to human fingerprints on atmospheric temperature. *Proc. Natl Acad. Sci. USA* **120**, e2300758120 (2023).
8. Stott, P. A., Sutton, R. T. & Smith, D. M. Detection and attribution of Atlantic salinity changes. *Geophys. Res. Lett.* **35**, L21702 (2008).
9. Santer, B. D. et al. Incorporating model quality information in climate change detection and attribution studies. *Proc. Natl Acad. Sci. USA* **106**, 14778–14783 (2009).
10. Terray, L. et al. Near-surface salinity as nature's rain gauge to detect human influence on the tropical water cycle. *J. Clim.* **25**, 958–977 (2012).
11. Pierce, D. W., Gleckler, P. J., Barnett, T. P., Santer, B. D. & Durack, P. J. The fingerprint of human-induced changes in the ocean's salinity and temperature fields. *Geophys. Res. Lett.* **39**, L21704 (2012).
12. Marvel, K. & Bonfils, C. Identifying external influences on global precipitation. *Proc. Natl Acad. Sci. USA* **110**, 19301–19306 (2013).
13. Gillett, N. P., Fyfe, J. C. & Parker, D. E. Attribution of observed sea level pressure trends to greenhouse gas, aerosol, and ozone changes. *Geophys. Res. Lett.* **40**, 2302–2306 (2013).
14. Christidis, N. & Stott, P. A. Changes in the geopotential height at 500 hPa under the influence of external climatic forcings. *Geophys. Res. Lett.* **42**, 10798–10806 (2015).
15. Barnett, T. P. et al. Penetration of human-induced warming into the world's oceans. *Science* **309**, 284–287 (2005).
16. Bilbao, R. A. F., Gregory, J. M., Bouttes, N., Palmer, M. D. & Stott, P. Attribution of ocean temperature change to anthropogenic and natural forcings using the temporal, vertical and geographical structure. *Clim. Dynam.* **53**, 5389–5413 (2019).
17. Santer, B. D. et al. Human influence on the seasonal cycle of tropospheric temperature. *Science* **361**, eaas8806 (2018).
18. Min, S.-K., Zhang, X., Zwiers, F. W. & Agnew, T. Human influence on Arctic sea ice detectable from early 1990s onwards. *Geophys. Res. Lett.* **35**, L21701 (2008).
19. Qian, C. & Zhang, X. Human influences on changes in the temperature seasonality in mid- to high-latitude land areas. *J. Clim.* **28**, 5908–5921 (2015).
20. Marvel, K. et al. Observed and projected changes to the precipitation annual cycle. *J. Clim.* **30**, 4983–4995 (2017).
21. Duan, J. et al. Detection of human influences on temperature seasonality from the nineteenth century. *Nat. Sustain.* **2**, 484–490 (2019).
22. Santer, B. D. et al. Robust anthropogenic signal identified in the seasonal cycle of tropospheric temperature. *J. Clim.* **35**, 6075–6100 (2022).
23. Dwyer, J. G., Biasutti, M. & Sobel, A. H. The effect of greenhouse gas-induced changes in SST on the annual cycle of zonal mean tropical precipitation. *J. Clim.* **27**, 4544–4565 (2014).
24. Alexander, M. A. et al. Projected sea surface temperatures over the 21st century: changes in the mean, variability and extremes for large marine ecosystem regions of Northern Oceans. *Elementa* **6**, 9 (2018).
25. Kwiatkowski, L. et al. Twenty-first century ocean warming, acidification, deoxygenation, and upper-ocean nutrient and primary production decline from CMIP6 model projections. *Biogeosciences* **17**, 3439–3470 (2020).
26. Timmermann, A., Jin, F. F. & Collins, M. Intensification of the annual cycle in the tropical Pacific due to greenhouse warming. *Geophys. Res. Lett.* **31**, L12208 (2004).
27. Sobel, A. H. & Camargo, S. J. Projected future seasonal changes in tropical summer climate. *J. Clim.* **24**, 473–487 (2011).
28. Chen, C. & Wang, G. Role of North Pacific mixed layer in the response of SST annual cycle to global warming. *J. Clim.* **28**, 9451–9458 (2015).
29. Jo, A. R. et al. Future amplification of sea surface temperature seasonality due to enhanced ocean stratification. *Geophys. Res. Lett.* **49**, e2022GL098607 (2022).
30. Liu, F., Lu, J., Luo, Y., Huang, Y. & Song, F. On the oceanic origin for the enhanced seasonal cycle of SST in the midlatitudes under global warming. *J. Clim.* **33**, 8401–8413 (2020).
31. Dwyer, J. G., Biasutti, M. & Sobel, A. H. Projected changes in the seasonal cycle of surface temperature. *J. Clim.* **25**, 6359–6374 (2012).
32. Capotondi, A., Alexander, M. A., Bond, N. A., Curchitser, E. N. & Scott, J. D. Enhanced upper ocean stratification with climate change in the CMIP3 models. *J. Geophys. Res. Oceans* **117**, C04031 (2012).
33. Li, G. et al. Increasing ocean stratification over the past half-century. *Nat. Clim. Change* **10**, 1116–1123 (2020).
34. Po-Chedley, S. et al. Natural variability contributes to model–satellite differences in tropical tropospheric warming. *Proc. Natl Acad. Sci. USA* **118**, e2020962118 (2021).
35. Po-Chedley, S. et al. Internal variability and forcing influence model–satellite differences in the rate of tropical tropospheric warming. *Proc. Natl Acad. Sci. USA* **119**, e2209431119 (2022).
36. Zelinka, M. D. et al. Causes of higher climate sensitivity in CMIP6 models. *Geophys. Res. Lett.* **47**, e2019GL085782 (2020).
37. Santer, B. D. et al. Identifying human influences on atmospheric temperature. *Proc. Natl Acad. Sci. USA* **110**, 26–33 (2013).
38. Solomon, S. et al. Emergence of healing in the Antarctic ozone layer. *Science* **353**, 269–274 (2016).
39. Fyfe, J. C., Kharin, V. V., Santer, B. D., Cole, J. N. S. & Gillett, N. P. Significant impact of forcing uncertainty in a large ensemble of climate model simulations. *Proc. Natl Acad. Sci. USA* **118**, e2016549118 (2021).
40. Meehl, G. A. et al. Context for interpreting equilibrium climate sensitivity and transient climate response from the CMIP6 Earth system models. *Sci. Adv.* **6**, eaba1981 (2020).
41. Deser, C. et al. Isolating the evolving contributions of anthropogenic aerosols and greenhouse gases: a new CESM1 large ensemble community resource. *J. Clim.* **33**, 7835–7858 (2020).
42. Shi, J.-R., Kwon, Y.-O. & Wijffels, S. E. Two distinct modes of climate responses to the anthropogenic aerosol forcing changes. *J. Clim.* **35**, 3445–3457 (2022).

43. Shi, J.-R., Kwon, Y. & Wijffels, S. E. Subsurface ocean temperature responses to the anthropogenic aerosol forcing in the North Pacific. *Geophys. Res. Lett.* **50**, e2022GL101035 (2023).
44. Ribes, A. & Terray, L. Application of regularised optimal fingerprinting to attribution. Part II: application to global near-surface temperature. *Clim. Dynam.* **41**, 2837–2853 (2013).
45. Marvel, K. et al. Do responses to different anthropogenic forcings add linearly in climate models? *Environ. Res. Lett.* **10**, 104010 (2015).
46. Maher, N., McGregor, S., England, M. H. & Gupta, A. S. Effects of volcanism on tropical variability. *Geophys. Res. Lett.* **42**, 6024–6033 (2015).
47. O'Brien, J. P. & Deser, C. Quantifying and understanding forced changes to unforced modes of atmospheric circulation variability over the North Pacific in a coupled model large ensemble. *J. Clim.* **36**, 19–37 (2023).
48. Deser, C., Simpson, I. R., Phillips, A. S. & McKinnon, K. A. How well do we know ENSO's climate impacts over North America, and how do we evaluate models accordingly? *J. Clim.* **31**, 4991–5014 (2018).
49. Fyfe, J. C., Saenko, O. A., Zickfeld, K., Eby, M. & Weaver, A. J. The role of poleward-intensifying winds on Southern Ocean warming. *J. Clim.* **20**, 5391–5400 (2007).
50. Shi, J.-R., Talley, L. D., Xie, S.-P., Liu, W. & Gille, S. T. Effects of buoyancy and wind forcing on Southern Ocean climate change. *J. Clim.* **33**, 10003–10020 (2020).
51. Shi, J.-R., Talley, L. D., Xie, S.-P., Peng, Q. & Liu, W. Ocean warming and accelerating Southern Ocean zonal flow. *Nat. Clim. Change* **11**, 1090–1097 (2021).

Methods

CMIP6 experiments and models

This study used output from climate model simulations performed under CMIP6 (ref. 52). We focused on ten CMIP6 models that performed all of the following four experiments: HIST and the single-forcing simulations AER, GHG and NAT[53]. Each of the ten models had multiple ensemble members. Each ensemble member of a given model was driven by the same external forcing, but had a different manifestation of natural internal climate variability superimposed on the underlying forced response. The number of ensemble members available for each model and each experiment is listed in Supplementary Table 1. For each experiment, there were 51 realizations in total. The MMM is the average of the ensemble means of these ten models. The piControl simulations from the same ten models were used for the purpose of estimating the noise from internal variability (see below).

We also analysed results from an experiment with forcing by stratospheric ozone changes only (O3). Only four of the ten models that performed HIST, GHG, AER and NAT simulations provided results for the O3 simulation (Supplementary Table 1).

The HIST, GHG, AER, O3 and NAT experiments covered the period from 1850 to 2014. We focused on the 1950–2014 period for comparing simulations with observations of changes in the amplitude of SST_{AC}. This choice of period was dictated by improvements in the spatial coverage and quality of observed SST data after World War II, as well as by large post-1950 changes in well-mixed GHGs, anthropogenic aerosols and stratospheric ozone. All model output was interpolated to a common, regular 1° × 1° grid.

Observations

We relied on four primary SST gridded products: HadISST[54], ERSST[55], COBE[56] and PCMDI[57]. ERSST and COBE are based on in situ measurements, and HadISST and PCMDI combine in situ and satellite estimates of SST. Different averaging and gap-filling approaches were employed to infill data-sparse regions and time periods in these gridded products. The HadISST and PCMDI datasets are not entirely independent: the PCMDI dataset is HadISST1 up to 1981, and uses the NOAA Optimum Interpolation SST data (OI.v2)[58] thereafter.

In addition to these observational SST products, we also used the monthly surface zonal wind from the latest-generation reanalysis of the European Centre for Medium-Range Weather Forecasts (ERA5)[59]. For the observed mixed layer depth (MLD), we first employed the gridded monthly temperature and salinity data from the IAP product[60] to calculate the potential density. MLD was then defined as the depth at which the ocean potential density exceeds the sea surface density at a criterion of $\delta\rho = 0.125$ kg m^{-3}, following the definition for MLD output (referred to as mlotst) from the CMIP6 models. There are likely to be substantial uncertainties in the IAP product arising from sparse measurements of the subsurface temperature and salinity fields in the Southern Ocean (particularly in the pre-Argo era of the IAP records).

We also used the information from ref. 61 to examine whether biases in ship SST data could be an important factor in our detection and attribution analysis. We found that it is unlikely that ship SST data biases could alter any of our findings regarding the identification of an SST_{AC} fingerprint in observations (not shown).

FAFMIP experiments

To isolate the individual effects of changes in wind stress and surface heat flux on SST_{AC} trends, we relied on output from the Flux-Anomaly-Forced Model Intercomparison (FAFMIP) experiments. Results are from five models: ACCESS-CM2, CanESM5, HadGEM3-GC31-LL, MIROC6 and MRI-ESM2-0. The FAFMIP experiments, branched from each model's piControl run, prescribe a set of surface flux perturbations for the ocean. These perturbations were obtained from the ensemble mean changes simulated at the time of doubled CO_2 by CMIP5 AOGCMs run under the 1pctCO2 scenario (in which atmospheric CO_2 levels increase by 1% each year). We examined three different FAFMIP experiments: FAF-all, in which perturbations of surface wind stress, surface freshwater flux and surface heat flux are simultaneously imposed; FAF-stress, with imposed perturbations of surface wind stress only; and FAF-heat, with imposed perturbations of net surface heat flux only[62].

All FAFMIP experiments considered here were run for 70 years. We show the anomalies of the 31–70 yr average relative to the climatology calculated from the full length of each model's piControl.

Calculation of annual cycle amplitudes

For each model simulation and observation product, and at each grid point x and year t, we performed a Fourier analysis on the 12 monthly mean values of SST. The amplitude of the first harmonic was taken as SST_{AC} (Extended Data Fig. 1d). Consistent with previous work[17], the first harmonic explained >95% of the total seasonal variance at almost all locations between 60° N and 60° S (except at regions close to the Equator). As an additional sensitivity study, we confirmed that our fingerprint results were insensitive to the definition of SST_{AC}. The S/N ratios and detection times obtained here with the first harmonic were very similar to those found when we defined SST_{AC} as the seasonal maximum SST minus the seasonal minimum SST at each grid point and in each year.

Pattern-based fingerprint analysis

Definition of the fingerprint. Detection methods generally require an estimate of the true, but unknown, climate change signal, typically designated as the fingerprint $F(x)$, in response to an individual forcing or set of forcings[63]. As in previous work, we assumed $F(x)$ to be the first EOF of the MMM change in SST_{AC} in the HIST simulations[17].

Let $S(i,j,x,t)$ represent SST_{AC} at grid point x and year t from the ith realization of the jth model's HIST simulation, where:

$i = 1,\ldots N_r(j)$ (the number of realizations for the jth model)

$j = 1,\ldots N_m$ (the number of models used in fingerprint estimation)

$x = 1,\ldots N_x$ (the total number of grid-points after regridding to a regular 1° × 1° grid)

$t = 1,\ldots N_t$ (the time in years)

Here, N_t varies across models (Supplementary Table 1). For HIST, $N_m = 10$ models. Before the fingerprint analysis, all model and observed SST_{AC} fields were interpolated to a common 1° × 1° latitude/longitude grid. The evolution of the MMM SST_{AC} was calculated by first averaging over an individual model's realizations (where multiple realizations were available), and then averaging across the number of models available for each experiment. MMM anomalies were then defined at each x and t with respect to the local MMM climatological annual cycle amplitude. The fingerprint is the first EOF of the changes over time in the MMM SST_{AC} anomalies from the HIST experiment—that is, the temporal changes in the annual cycle of SST. To minimize the impact of sea ice on SST_{AC}, the domain was restricted to 60° N–60° S and to regions where the winter sea-ice concentration is less than 10%. The anomalies were weighted by the square root of the cosine of the grid node's latitude[64] before calculating the EOF. Most of the discussion focuses on model fingerprints estimated over 1950–2014. We also calculated fingerprints for three additional analysis periods (1960–2014, 1970–2014 and 1980–2014). As noted in the main text, the spatial structure of the fingerprint patterns did not change markedly over these periods (Extended Data Fig. 2).

Fingerprint detection. We seek to determine whether the pattern similarity between the time-varying observations and $F(x)$ shows a statistically significant increase over time. To address this question, we required control run estimates of internally generated variability (noise), in which we knew a priori that there was no expression of the fingerprint, except by chance.

This intrinsic noise was estimated using piControl output from the same ten models employed to calculate the HIST fingerprint. These

control simulations can be affected by residual long-term drift. To reduce the effects of such drift on estimates of the internal variability of SST_{AC}, we fitted a cubic polynomial to the full length of each model's control run and then removed the fitted polynomial[65,66]. Fitting and drift removal was performed at each model grid point. Because the individual model control runs were of unequal length, our noise estimates relied on the past 400 years of each model's piControl run. This yielded a total of 4,000 years of concatenated control run data, and avoided introducing any bias associated with differing control run lengths.

Observed SST_{AC} estimates are expressed as anomalies relative to climatological means over the 1950–2014 analysis period (or over the alternate analysis periods in Fig. 2c). The observed temperature data were projected onto $F(x)$ to obtain signal time series $Z_o(t)$:

$$Z_o(t) = \sum_{x=1}^{N_x} O(x,t)\, F(x) \quad (1)$$

where $O(x, t)$ are the observed SST_{AC} anomalies. This projection is equivalent to a spatially uncentred covariance between the patterns $O(x, t)$ and $F(x)$ at year t. The signal time series $Z_o(t)$ provides information on the fingerprint strength in the observations. If observed patterns of temperature change are becoming increasingly similar to $F(x)$, $Z_o(t)$ should increase over time.

To assess whether this increase was statistically significant, we compared trends in $Z_o(t)$ with a null distribution for which we knew a priori that there was no expression of the fingerprint, except by chance. We derived this null distribution using $C(x, t)$, the 4,000 yr concatenated noise dataset, generated from the piControl runs as described above. The noise time series from the control model run $N_c(t)$ is the projection of $C(x, t)$ onto the fingerprint:

$$N_c(t) = \sum_{x=1}^{N_x} C(x,t)\, F(x) \quad (2)$$

where the length of $N_c(t)$ is 4,000 years (see above).

We estimated S/N ratios by fitting least-squares linear trends of increasing length L years to $Z_o(t)$, and then comparing these trends with the standard deviation of the distribution of maximally overlapping L-length trends in $N_c(t)$ (refs. 17,37). Signal detection was stipulated to occur when the trend in $Z_o(t)$ exceeded and remained above the stipulated significance level (which was 5% in our study)[22]. The test was one-tailed, and we assumed a Gaussian distribution of trends in $N_c(t)$. The start date for fitting linear trends to $Z_o(t)$ was 1950 for our baseline analysis, and 1960, 1970 and 1980 in the alternate analysis periods shown in Fig. 2c. We used a minimum trend length of 10 years, so the first S/N ratio (and the earliest possible detection time in the baseline period) was for 10 yr trends ending in 1959.

We also show S/N results that are based solely on model simulation output. In our model-only results, $N_c(t)$ was calculated as in equation (2), but the observational estimates in equation (1) were replaced by $S(i, j, x, t)$, the annual cycle amplitude information from each of the 51 HIST simulations (grey curves in Figs. 1f and 2b).

HIST fingerprint versus single-forcing fingerprints. As noted in the main text, we employed two methods to study the contributions of individual external forcings (GHG, AER, NAT and O3) to the simulated SST_{AC} changes. In Method 1, SST_{AC} anomalies from individual realizations of the four single-forcing simulations were projected onto the common fingerprint calculated from the HIST MMM. As in the case of HIST, the MMMs of SST_{AC} from these four single-forcing experiments were also projected onto $F(x)$.

In Method 2, we projected SST_{AC} changes from the HIST MMM and from individual HIST realizations onto each of the four fingerprints estimated from the GHG, AER, O3 and NAT multi-model average SST_{AC} changes. This yielded information on the strength of each individual fingerprint in the historical all-forcing simulations, and on how the strength of the GHG, AER, O3 and NAT fingerprints evolved with increasingly longer analysis periods.

We used EOF1 for the Method 2 GHG fingerprint and EOF2 for the Method 2 fingerprints from AER, O3 and NAT (Supplementary Fig. 1). This choice was made because in the GHG simulation, EOFs 1 and 2 were clearly separated in terms of explained variance, with the explained variance associated with GHG EOF1 a factor of three larger than the explained variance of GHG EOF2. The latter pattern largely reflected tropical internal variability associated with the El Niño/Southern Oscillation. In contrast, EOFs 1 and 2 were less well separated in terms of the explained variance in the AER, O3 and NAT simulations—their EOF1 was very similar to EOF2 from the GHG simulation, whereas the EOF2 patterns of AER, O3 and NAT were dominated by extratropical forced responses. The temporal evolution of the first and second principal components (PC1 and PC2, respectively) was consistent with this interpretation (Supplementary Fig. 1i,j). GHG PC1 showed a large increase in amplitude over 1950–2014, whereas the PC1 of AER, O3 and NAT were dominated by interannual variability. Clearer long-term trends are evident in the PC2 of AER and O3, while PC2 in NAT exhibited large decreases immediately after major volcanic eruptions.

SST_{AC} from observations and HIST runs was projected onto these four single-forcing fingerprints (Supplementary Fig. 2). For the projections onto the GHG fingerprint, all 51 model HIST realizations and three of the four observational datasets eventually exceeded the 5% significance threshold. S/N levels were systematically lower for the AER, NAT and O3 fingerprints, which were therefore not as clearly identifiable in the HIST realizations or observations as the GHG fingerprint. This provides support for a key finding from our Method 1 analysis: forcing by well-mixed GHGs was the dominant factor in the identification of externally forced changes in SST_{AC}.

We note that in Method 2, the NAT fingerprint was identifiable at the 5% level in 88% of the HIST realizations and in two of the four observed SST_{AC} datasets (Supplementary Fig. 2d). While there were small changes over time in the solar and volcanic forcing over 1950–2014[39], the behaviour of PC1 of the NAT SST_{AC} changes (Supplementary Fig. 1i) suggested that NAT forcing is unlikely to produce a significant multi-decadal trend in SST_{AC}. Instead, the identification of the NAT fingerprint in the HIST SST_{AC} data appears to be due to the spatial similarity between certain large-scale features of the GHG and NAT fingerprints (compare Supplementary Fig. 1a,f). Thus in Method 2 (which we do not focus on in our fingerprint analysis) the statistical problem of degeneracy[67] of the normalized GHG and NAT fingerprints hampered reliable assessment of the relative contributions of GHG and NAT forcing to the simulated SST_{AC} changes. In Method 1, however, the larger amplitude of the SST_{AC} response to GHG forcing (relative to NAT forcing) was preserved, which is why the HIST fingerprint could be identified in the individual GHG realizations, but not in the individual NAT realizations.

The uncentred pattern correlation between GHG EOF1 and NAT EOF2 was higher than the pattern correlations between GHG EOF1 and the EOF2 patterns of other single-forcing experiments (Supplementary Table 2). This similarity may arise from major tropical volcanic eruptions in the 1950–2014 analysis period (Agung, El Chichón and Pinatubo) and the associated shifts of the intertropical convergence zone[68], which in turn could affect the latitudinal location of regions of mid-latitude increases in SST_{AC}.

Simplified mixed-layer heat budget analysis

Our mixed-layer heat budget model is a simplified version of the traditional mixed-layer heat budget model that takes into account only the dominant heat fluxes and MLD affecting the temperature of the oceanic mixed layer:

$$\frac{dT}{dt} \approx \frac{Qnet - Qb}{\rho \times Cp \times MLD} \quad (3)$$

The left-hand side is the ocean temperature (T) tendency, and the right-hand side is the estimate based on Qnet, Qb and MLD. These terms are functions of month, latitude and longitude and are calculated from HIST runs. The terms ρ and Cp are the density and specific heat of seawater, respectively.

For the changes in the annual cycle (AC) amplitude of dT/dt:

$$\mathrm{AC}\left(\frac{\mathrm{d}T_2}{\mathrm{d}t}\right)-\mathrm{AC}\left(\frac{\mathrm{d}T_1}{\mathrm{d}t}\right)\approx \mathrm{AC}\left(\frac{\mathrm{Qnet}_2-\mathrm{Qb}_2}{\rho\times \mathrm{Cp}\times \mathrm{MLD}_2}\right)-\mathrm{AC}\left(\frac{\mathrm{Qnet}_1-\mathrm{Qb}_1}{\rho\times \mathrm{Cp}\times \mathrm{MLD}_1}\right) \quad (4)$$

where '1' represents the average of the period 1950–1979 and '2' represents the average of the period 1985–2014. The changes are the difference between these two 30 yr periods. We also held Qnet and MLD constant in equation (4) to isolate the effects due to MLD change and Qnet change:

$$\Delta\mathrm{MLD\ effect}=\mathrm{AC}\left(\frac{\mathrm{Qnet}_1-\mathrm{Qb}_1}{\rho\times \mathrm{Cp}\times \mathrm{MLD}_2}\right)-\mathrm{AC}\left(\frac{\mathrm{Qnet}_1-\mathrm{Qb}_1}{\rho\times \mathrm{Cp}\times \mathrm{MLD}_1}\right) \quad (5)$$

$$\Delta\mathrm{Qnet\ effect}=\mathrm{AC}\left(\frac{\mathrm{Qnet}_2-\mathrm{Qb}_2}{\rho\times \mathrm{Cp}\times \mathrm{MLD}_1}\right)-\mathrm{AC}\left(\frac{\mathrm{Qnet}_1-\mathrm{Qb}_1}{\rho\times \mathrm{Cp}\times \mathrm{MLD}_1}\right) \quad (6)$$

In equations (5) and (6), the Qb and Qnet terms are for the same analysis period. Results are insensitive to whether Qb is chosen from period 1 or period 2.

We examined the effect of MLD change in terms of its absolute change (equation (7)) and relative change (equation (8)). As shown in equation (7), we assumed a summer MLD change to be added to all the months from the base period. In terms of relative change, MLD was assumed to shoal by 5% everywhere and in every month relative to the background value (equation (8)).

$$\Delta\mathrm{MLD}_{\mathrm{summer}}\ \mathrm{effect}=\mathrm{AC}\left(\frac{\mathrm{Qnet}_1-\mathrm{Qb}_1}{\rho\times \mathrm{Cp}\times(\mathrm{MLD}_1+(\mathrm{MLD}_{2,\mathrm{summer}}-\mathrm{MLD}_{1,\mathrm{summer}}))}\right)-\mathrm{AC}\left(\frac{\mathrm{Qnet}_1-\mathrm{Qb}_1}{\rho\times \mathrm{Cp}\times \mathrm{MLD}_1}\right) \quad (7)$$

$$\Delta\mathrm{MLD}_{5\%\mathrm{shoaling}}\ \mathrm{effect}=\mathrm{AC}\left(\frac{\mathrm{Qnet}_1-\mathrm{Qb}_1}{\rho\times \mathrm{Cp}\times(\mathrm{MLD}_1\times 0.95)}\right)-\mathrm{AC}\left(\frac{\mathrm{Qnet}_1-\mathrm{Qb}_1}{\rho\times \mathrm{Cp}\times \mathrm{MLD}_1}\right) \quad (8)$$

Data availability

The CMIP6 historical, single-forcing and FAFMIP simulation outputs are available via the Earth System Grid of the Program for Climate Model Diagnosis and Intercomparison (PCMDI): https://esgf-node.llnl.gov/search/cmip6/. HadISST data are available at: https://www.metoffice.gov.uk/hadobs/hadisst. ERSST data are available at: https://www.ncei.noaa.gov/products/extended-reconstructed-sst. COBE data are available at: https://psl.noaa.gov/data/gridded/data.cobe2.html. PCMDI data are available at: https://doi.org/10.22033/ESGF/input4MIPs.16921. ERA5 data are available at: https://www.ecmwf.int/en/forecasts/dataset/ecmwf-reanalysis-v5. IAP data are available at: https://climatedataguide.ucar.edu/climate-data/ocean-temperature-analysis-and-heat-content-estimate-institute-atmospheric-physics. The processed data are available via Figshare at https://doi.org/10.6084/m9.figshare.23271569 (ref. 69).

References

52. Eyring, V. et al. Overview of the Coupled Model Intercomparison Project Phase 6 (CMIP6) experimental design and organization. *Geosci. Model Dev.* **9**, 1937–1958 (2016).
53. Gillett, N. P. et al. The Detection and Attribution Model Intercomparison Project (DAMIP v1.0) contribution to CMIP6. *Geosci. Model Dev.* **9**, 3685–3697 (2016).
54. Rayner, N. A. et al. Global analyses of sea surface temperature, sea ice, and night marine air temperature since the late nineteenth century. *J. Geophys. Res. Atmos.* **108**, 4407 (2003).
55. Huang, B. et al. Extended Reconstructed Sea Surface Temperature, Version 5 (ERSSTv5): upgrades, validations, and intercomparisons. *J. Clim.* **30**, 8179–8205 (2017).
56. Hirahara, S., Ishii, M. & Fukuda, Y. Centennial-scale sea surface temperature analysis and its uncertainty. *J. Clim.* **27**, 57–75 (2014).
57. Durack, P. J., Taylor, K. E., Ames, S., Po-Chedley, S. & Mauzey, C. *PCMDI AMIP SST and Sea-Ice Boundary Conditions Version 1.1.8* (Earth System Grid Federation, 2022); https://doi.org/10.22033/ESGF/input4MIPs.16921
58. Reynolds, R. W., Rayner, N. A., Smith, T. M., Stokes, D. C. & Wang, W. An improved in situ and satellite SST analysis for cimate. *J. Clim.* **15**, 1609–1625 (2002).
59. Hersbach, H. et al. The ERA5 global reanalysis. *Q. J. R. Meteorol. Soc.* **146**, 1999–2049 (2020).
60. Cheng, L. et al. Improved estimates of ocean heat content from 1960 to 2015. *Sci. Adv.* **3**, e1601545 (2017).
61. Chan, D. & Huybers, P. Correcting observational biases in sea surface temperature observations removes anomalous warmth during World War II. *J. Clim.* **34**, 4585–4602 (2021).
62. Gregory, J. M. et al. The Flux-Anomaly-Forced Model Intercomparison Project (FAFMIP) contribution to CMIP6: investigation of sea-level and ocean climate change in response to CO_2 forcing. *Geosci. Model Dev.* **9**, 3993–4017 (2016).
63. Hasselmann, K. *On the Signal-To-Noise Problem in Atmospheric Response Studies* (Royal Meteorological Society, 1979).
64. Van Den Dool, H. M., Saha, S. & Johansson, Å. Empirical orthogonal teleconnections. *J. Clim.* **13**, 1421–1435 (2000).
65. Irving, D. B., Wijffels, S. & Church, J. A. Anthropogenic aerosols, greenhouse gases, and the uptake, transport, and storage of excess heat in the climate system. *Geophys. Res. Lett.* **46**, 4894–4903 (2019).
66. Shi, J.-R., Wijffels, S. E., Kwon, Y. & Xie, S. Interhemispheric contrasts of ocean heat content change reveals distinct fingerprints of anthropogenic climate forcings. *Geophys. Res. Lett.* **50**, e2023GL102741 (2023).
67. Allen, M. R. & Tett, S. F. B. Checking for model consistency in optimal fingerprinting. *Clim. Dynam.* **15**, 419–434 (1999).
68. Bonfils, C. J. W. et al. Human influence on joint changes in temperature, rainfall and continental aridity. *Nat. Clim. Change* **10**, 726–731 (2020).
69. Shi, J.-R., Santer, B. D., Kwon, Y.-O. & Wijffels, S. E. The emerging human influence on the seasonal cycle of sea surface temperature. *Figshare* https://doi.org/10.6084/m9.figshare.23271569 (2024).

Acknowledgements

We acknowledge the World Climate Research Programme's Working Group on Coupled Modelling, which led the design of CMIP6 and coordinated the work, and we also thank individual climate modelling groups (listed in Supplementary Table 1) for their efforts in performing all of the model simulations analysed here. J.-R.S., Y.-O.K. and S.E.W. are supported by US National Science Foundation under grant number OCE-2048336. B.D.S. and Y.-O.K. were supported by the Francis E. Fowler IV Center for Ocean and Climate at Woods Hole Oceanographic Institution (WHOI).

Author contributions

J.-R.S. and B.D.S. conceived the study. J.-R.S. conducted the analysis and wrote the first draft. J.-R.S., B.D.S., Y.-O.K. and S.E.W. contributed to interpreting the results, writing and editing the manuscript.

Competing interests
The authors declare no competing interests.

Additional information
Extended data is available for this paper at https://doi.org/10.1038/s41558-024-01958-8.

Supplementary information The online version contains supplementary material available at https://doi.org/10.1038/s41558-024-01958-8.

Correspondence and requests for materials should be addressed to Jia-Rui Shi or Benjamin D. Santer.

Peer review information *Nature Climate Change* thanks Masami Nonaka and the other, anonymous, reviewer(s) for their contribution to the peer review of this work.

https://doi.org/10.1038/s41558-024-01958-8

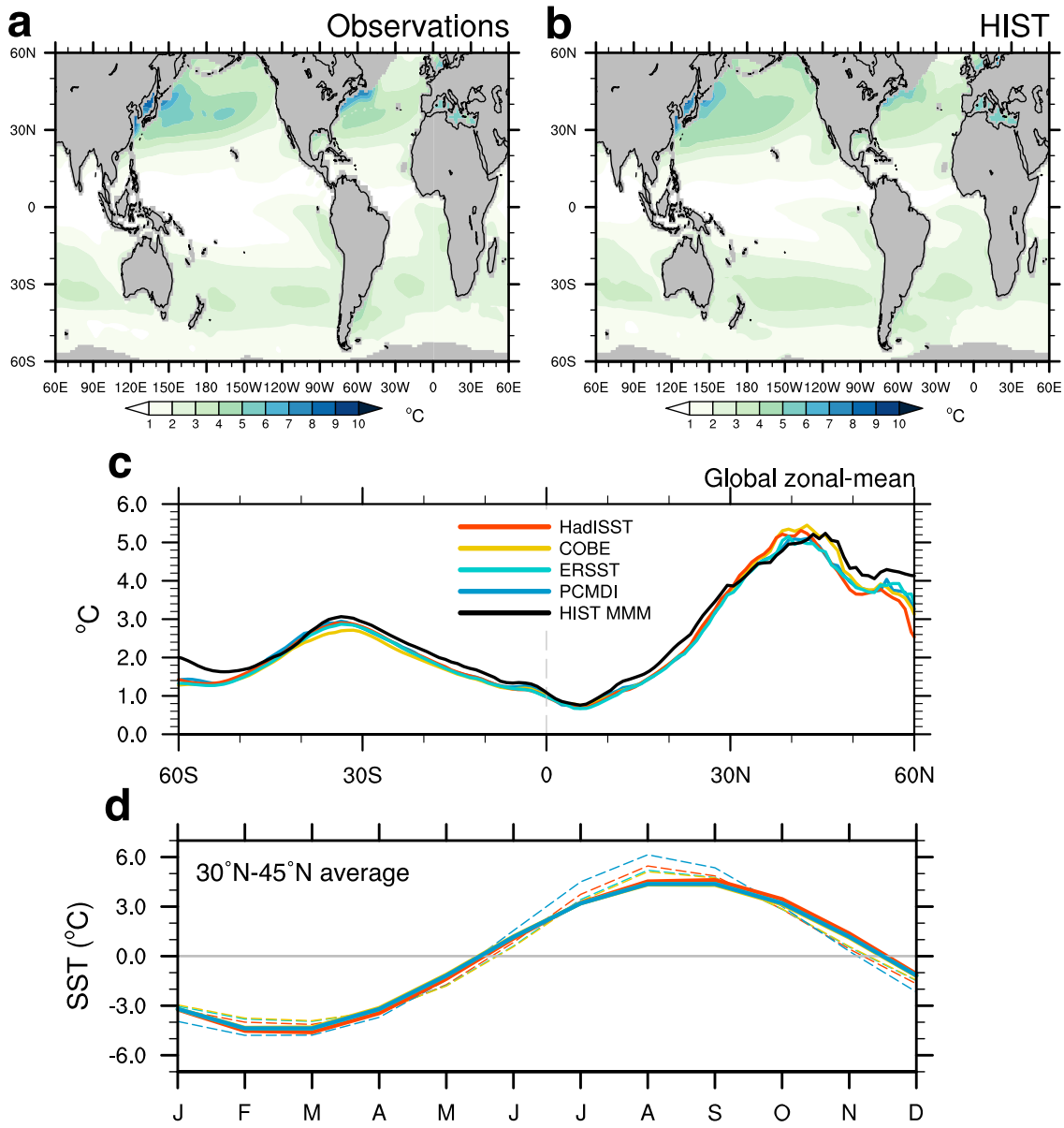

Extended Data Fig. 1 | Spatial patterns and zonal mean of the climatology of SST annual cycle amplitude (SST_{AC}) from four different observational products and from the multi-model mean (MMM) of the HIST simulations. **a** Average of four different observed SST datasets. **b** HIST MMM. **c** Zonal-mean climatology of the HIST MMM and individual observed SST datasets. **d** Monthly climatology of SST averaged between 30˚N-45˚N from observations (dashed curves) and the fits of the first harmonic obtained through Fourier analysis (solid curves). Results are calculated over 1950 to 2014.

https://doi.org/10.1038/s41558-024-01958-8

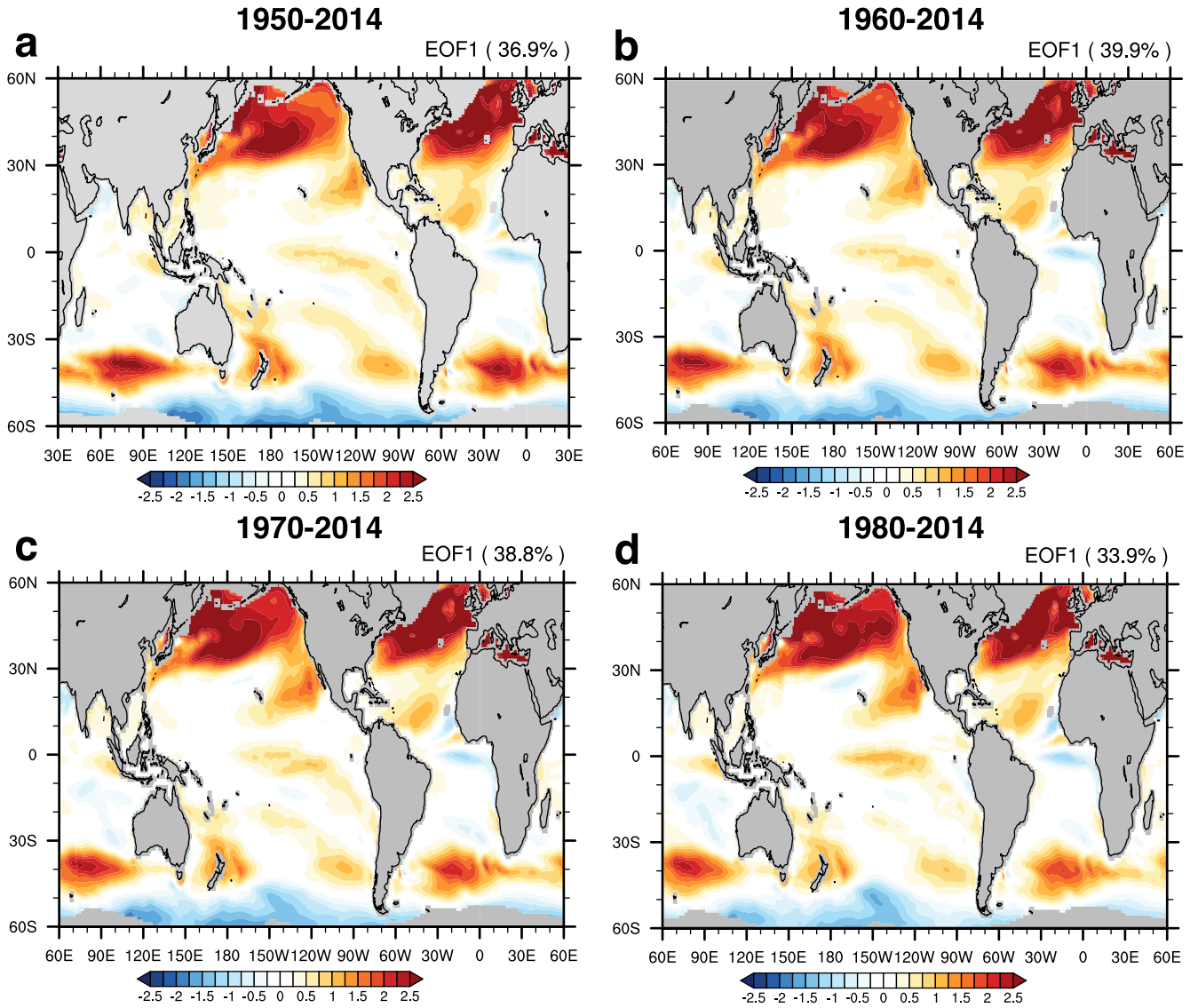

Extended Data Fig. 2 | Leading EOF of SST_{AC} estimated from the HIST MMM. a-d Results for four different analysis periods. The explained variances are shown in brackets.

https://doi.org/10.1038/s41558-024-01958-8

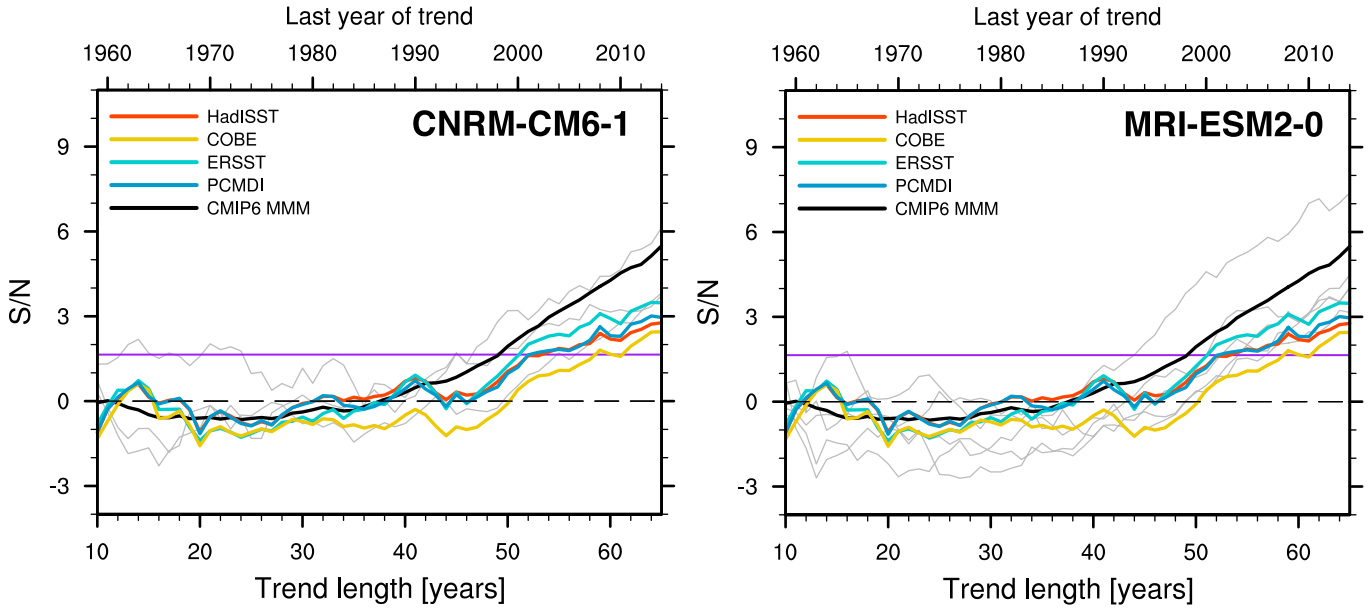

Extended Data Fig. 3 | S/N ratios from two selected CMIP6 models. Results are as in Fig. 2b, but the 'model only' S/N ratios here (in grey) are from two models only: CNRM-CM6-1 and MRI-ESM2-0. Individual realizations from each model can have appreciable differences in their S/N behavior.

https://doi.org/10.1038/s41558-024-01958-8

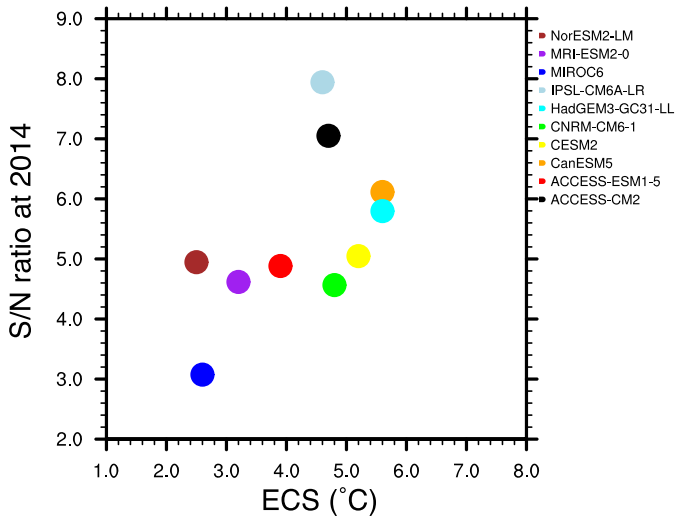

Extended Data Fig. 4 | Scatterplot between the climate sensitivity of the 10 CMIP6 models analyzed here and the final value of the S/N ratio for the 65-year analysis period from 1950 to 2014. The effective climate sensitivities are based on the results from ref. 40. The correlation between ECS and S/N ratio at 2014 is 0.55.

https://doi.org/10.1038/s41558-024-01958-8

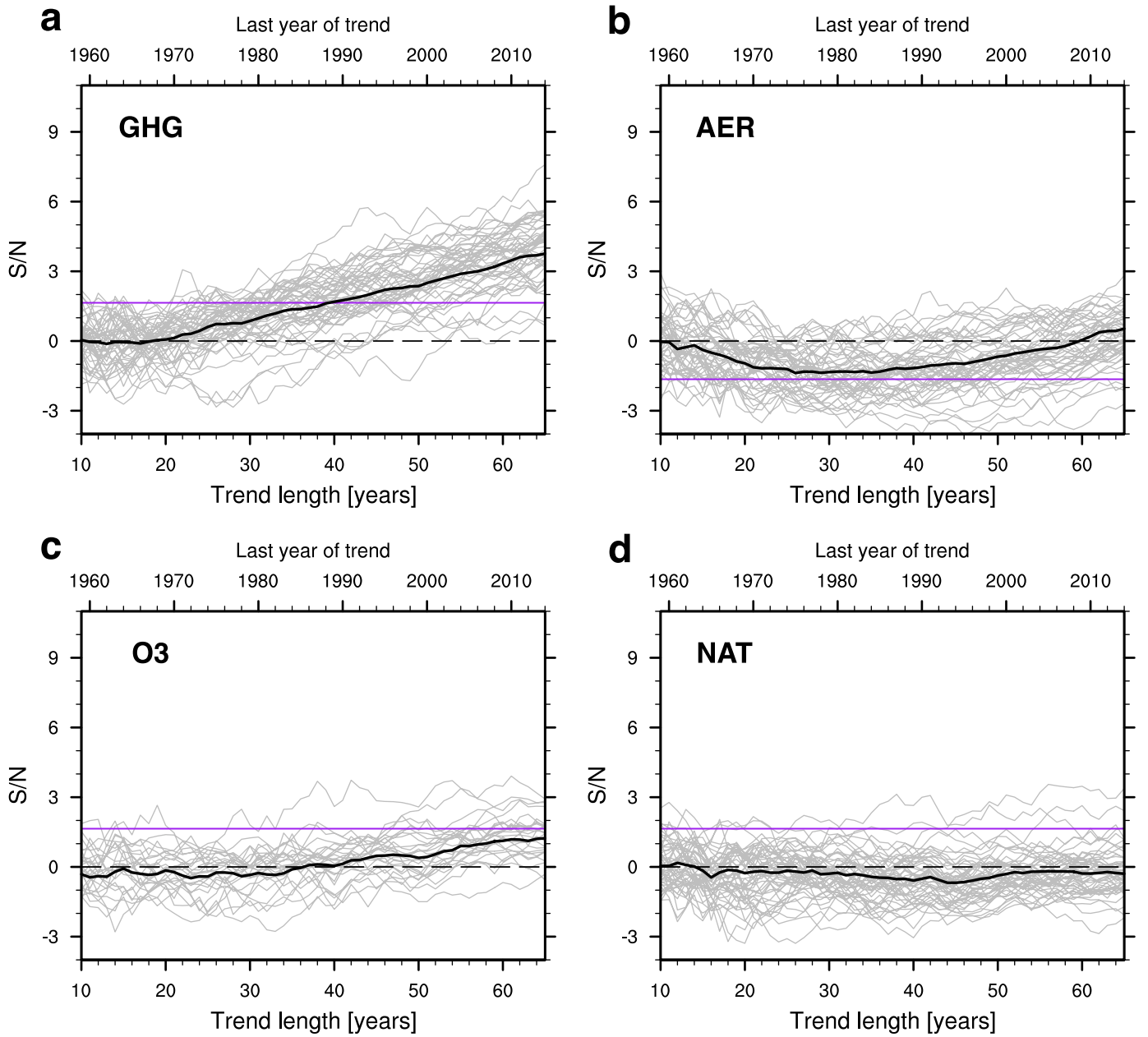

Extended Data Fig. 5 | S/N ratios from the GHG, AER, O3, and NAT single-forcing runs. Results are based on use of the same HIST fingerprint, which is searched for in the SST_{AC} changes of each single-forcing run (Method 1). **a**–**d** MMM result (the black curve) from GHG (**a**), AER (**b**), O3 (**c**) and NAT (**d**) single-forcing runs and results from individual realizations (the grey curves). GHG, AER, and NAT results are from 10 models with a total of 51 realizations; only four models with a total of 26 realizations were available for calculating O3 S/N ratios. The horizontal purple line is the 5% significance level. For further details refer to Methods.

https://doi.org/10.1038/s41558-024-01958-8

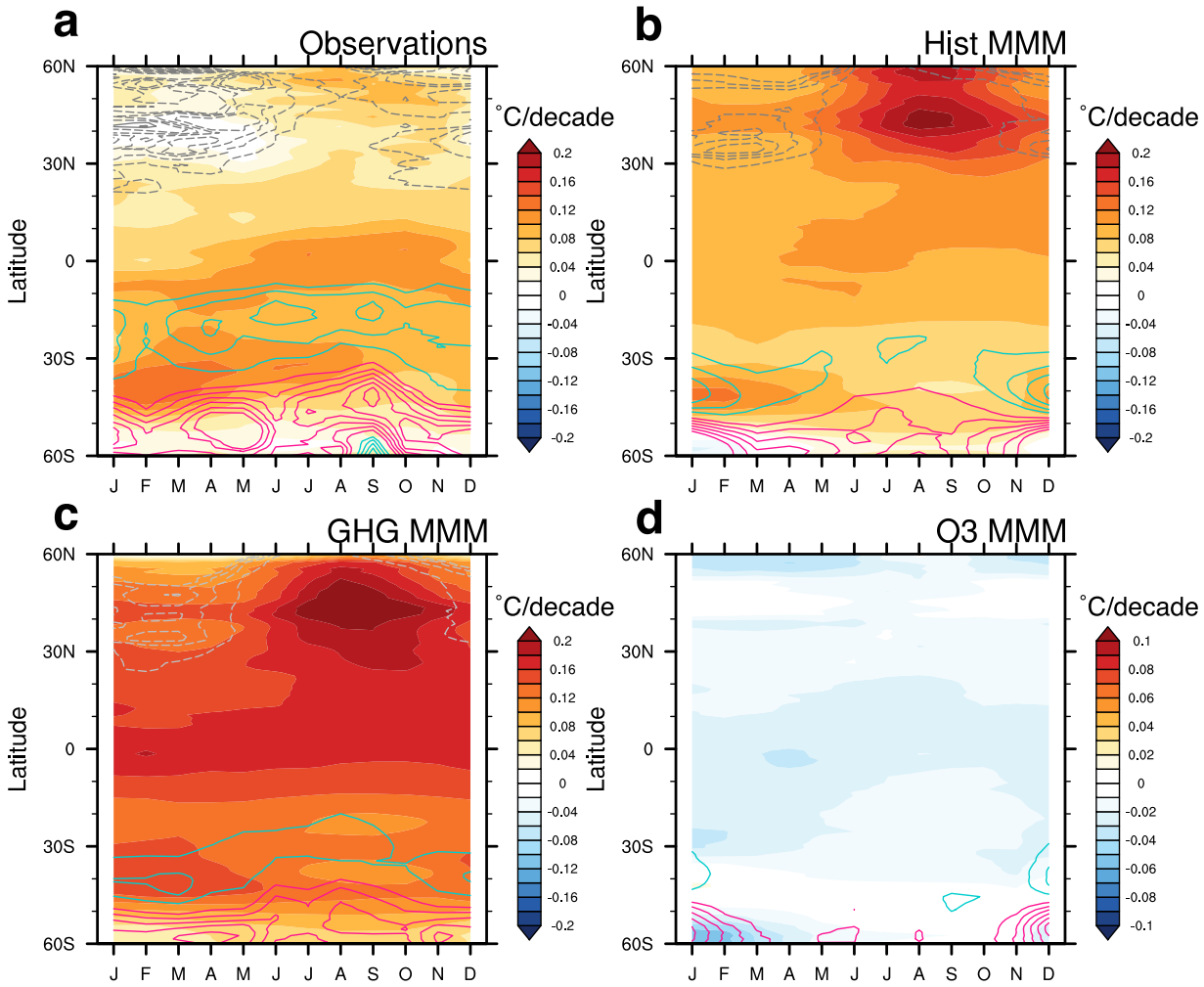

Extended Data Fig. 6 | Zonal-mean monthly-mean SST trends over 1950 to 2014. a The ensemble mean of four observed datasets. **b-d** The MMM of the HIST, GHG, and O3 simulations. In contrast to Fig. 4, the trends are not expressed as departures from annual-mean trends.

https://doi.org/10.1038/s41558-024-01958-8

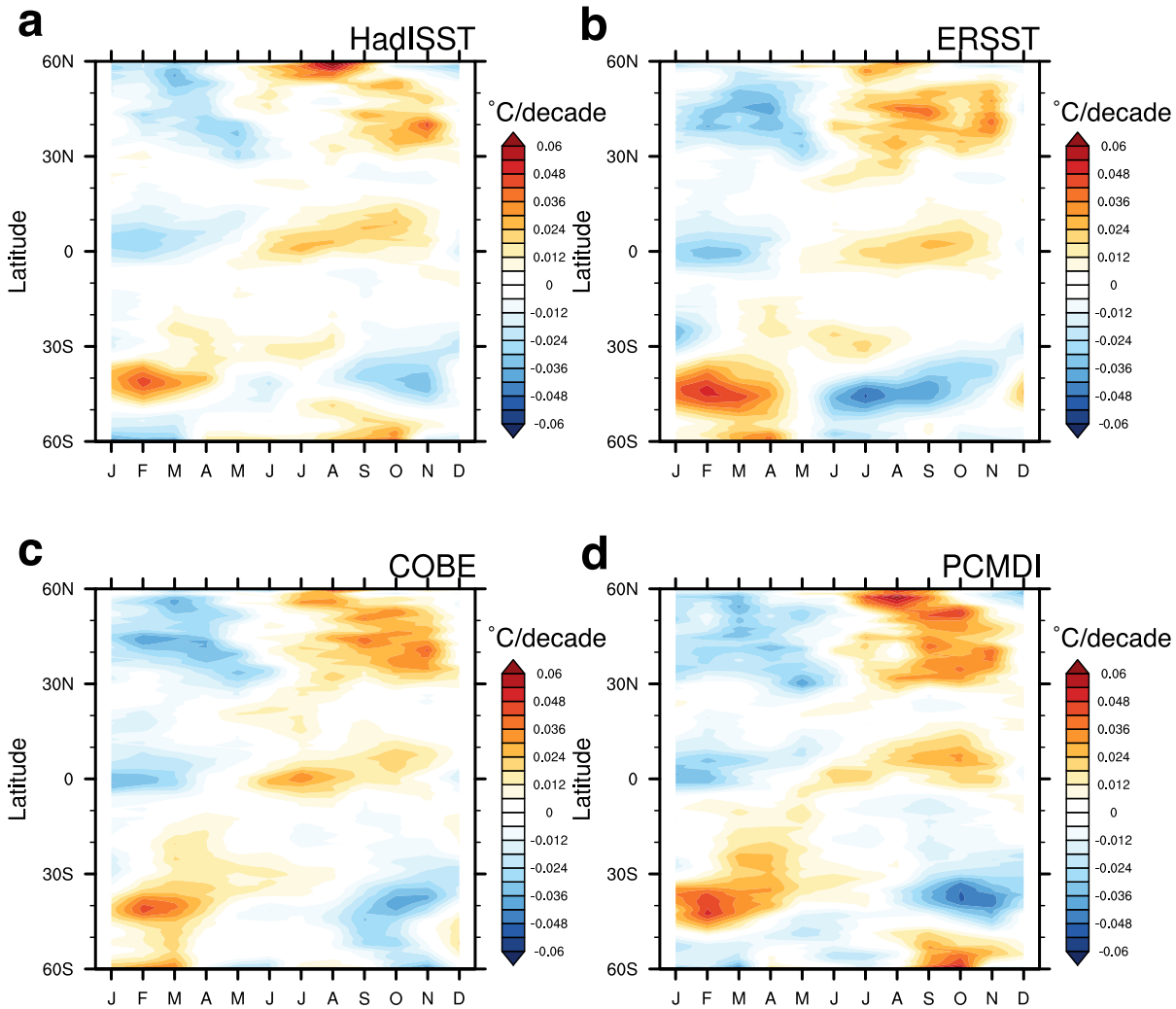

Extended Data Fig. 7 | Zonal-mean monthly-mean SST trends over 1950 to 2014 in four observed datasets. a-d Results from four observed datasets: HadISST (**a**), ERSST (**b**), COBE (**c**) and PCMDI (**d**). The results are expressed as departures from annual-mean trends.

https://doi.org/10.1038/s41558-024-01958-8

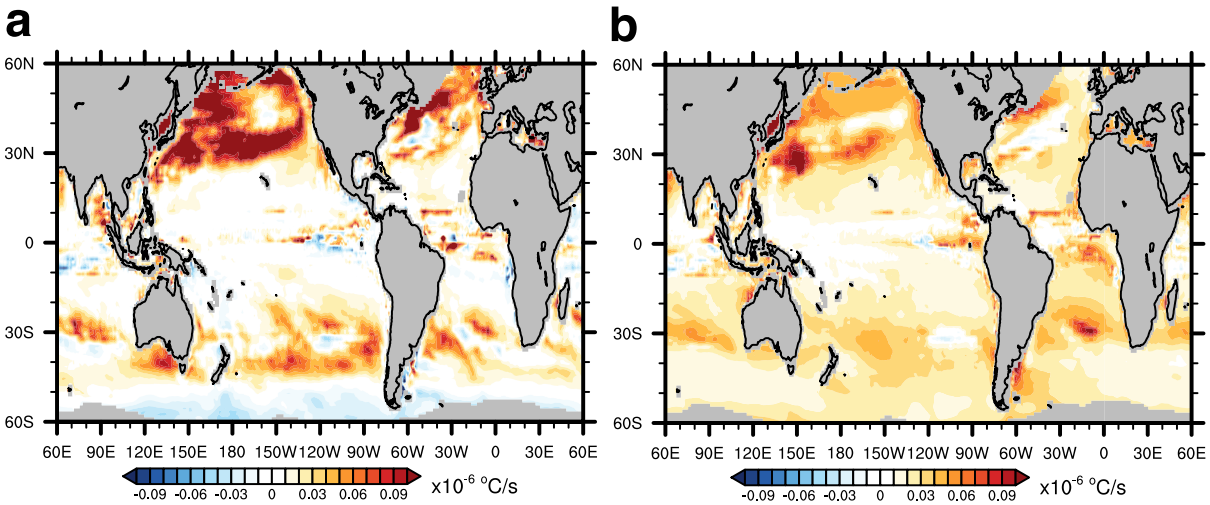

Extended Data Fig. 8 | Changes of annual cycle amplitude of SST tendency between 1950–1979 and 1985–2014 due to MLD changes. a Changes of annual cycle when it is assumed to have a consistent summer MLD change for all 12 months (see Eq. 7). **b** Changes of annual cycle when MLD is assumed to shoal by 5% at every location and in every month relative to the background monthly value (see Eq. 8).

https://doi.org/10.1038/s41558-024-01958-8

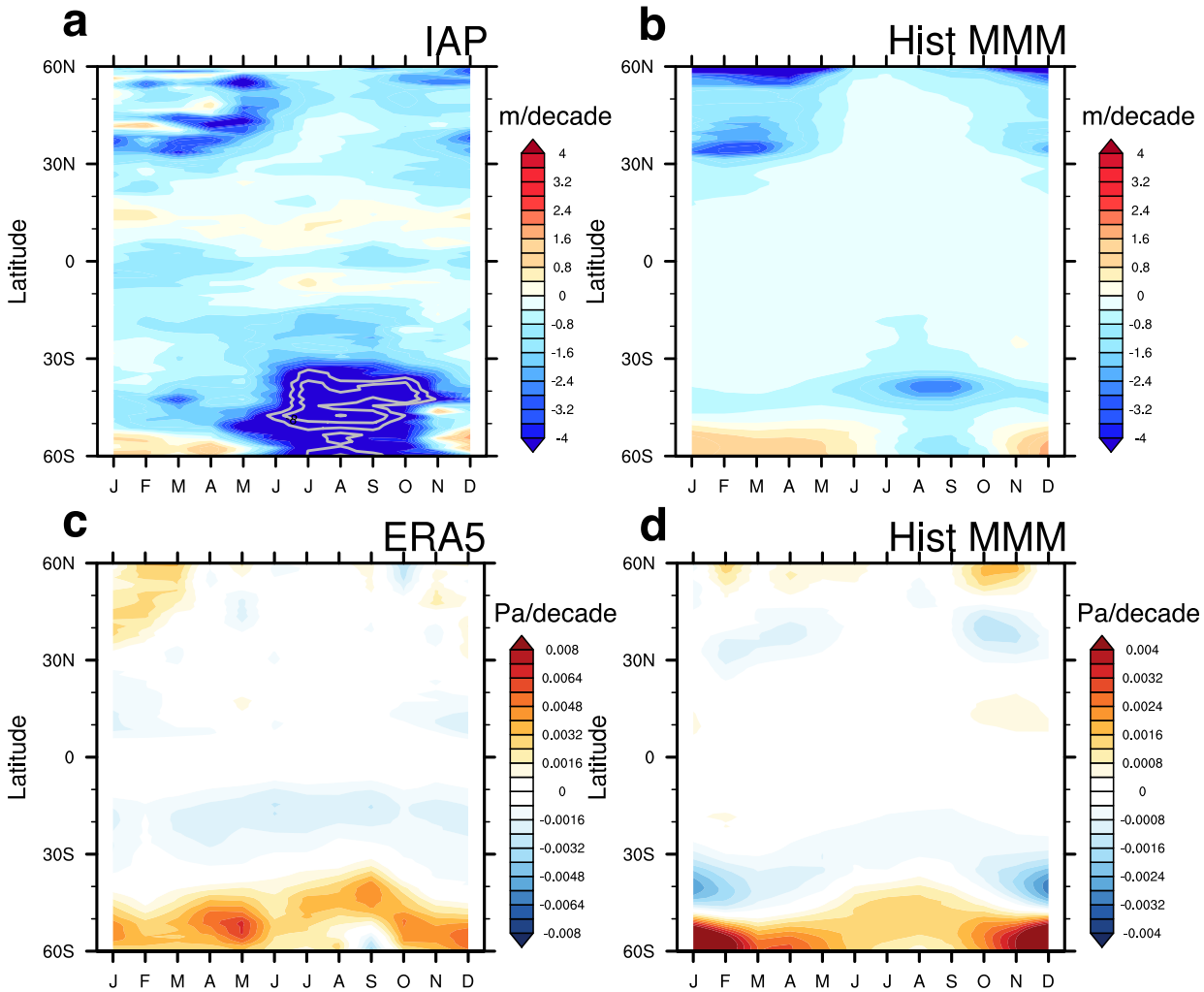

Extended Data Fig. 9 | Zonal-mean monthly-mean trends over 1950 to 2014 in MLD and zonal wind stress. a-b MLD trends from the IAP product and the MMM of the HIST simulations, respectively. Grey contours highlight the large MLD trends of −6 and −8 m/decade. **c-d** Zonal wind stress trends from ERA5 and the MMM of the HIST simulations.